

Proceedings of the Second
International Postgraduate
Conference on Infrastructure and
Environment

(Supplement)

Organized by

Faculty of Construction and Land Use
The Hong Kong Polytechnic University

Editors:
LIU Qian, Cathy
OU Yang, Yang
QU Minglu, Lulu
SUN Ke, Daniel
TANG Liyaning, Maggie
TAO Li, Lisa
WANG Yuru, Rachel
ZENG Cheng, Henry
ZHANG Yuexin, Cindy

All rights reserved. No part of this publication may be reproduced, stored and transmitted in any form, or by any means without prior written permission from the editors.

The views expressed in the papers are of the individual authors. The editors are not liable to anyone for any loss or damage caused by any error or omission in the papers, whether such error or omission is the result of negligence or any other cause. All and such liability is disclaimed.

ISBN: 978-988-17311-5-9

© 2010 Faculty of Construction and Land Use, The Hong Kong Polytechnic University

TABLE OF CONTENTS

Environmental Technology and Management

POLYHYDROXYALKANOATES (PHA) PRODUCTION IN ACTIVATED SLUDGE FED BY VOLATILE FATTY ACIDS ZHONG D., WANG Y.J., HE D., SIN S.N., CHUA H.....	1
---	---

Structural Engineering

FINITE ELEMENT ANALYSIS OF FRP WRAPS IN SPLIT-DISK TESTS S.Q. LI, J.F. CHEN, L.A. BISBY.....	9
LONG-TERM MONITORING FOR SOIL NAILS AND ANCHORS BASED ON FBG SENSING TECHNIQUE H.F. PEI, J.H. YIN, C.Y. HONG, H.H. ZHU.....	16
MEASUREMENT OF CRACKS IN CONCRETE BEAMS USING A BRILLOUIN OPTICAL TIME DOMAIN ANALYSIS SENSING TECHNOLOGY C.Y. HONG, J.H. YIN, H.F. PEI, D. HUANG.....	22

Environmental Technology and Management

POLYHYDROXYALKANOATES (PHA) PRODUCTION IN ACTIVATED SLUDGE FED BY VOLATILE FATTY ACIDS

Zhong D., Wang Y.J., He D., Sin S.N., Chua H.

Department of Civil and Structure Engineering, The Hong Kong Polytechnic University, Hong Kong

ABSTRACT

To reduce the production cost of polyhydroxyalkanoates (PHA) and disposal amount of excess sludge simultaneously, the feasibility of using fermentative volatile fatty acids (VFAs) as carbon sources to synthesize PHA by activated sludge was examined. At pH 11.0 and fermentative time of 7 day, the volatile fatty acids (VFAs) yield was 258.65 mgTOC/gVSS. To restrain cell growth during PHA production, the released phosphorus and residual ammonium in the fermentative VFAs was recovered by the formation of struvite precipitation. Acetic acid was the predominant composition of the fermentative VFAs. PHA accumulation in excess sludge occurred feeding by fermentative VFAs with aerobic dynamic feeding process. The maximum PHA content accounted for 56.5% of the dry cell. It can be concluded from this study that the VFAs generated from excess sludge fermentation were a suitable carbon source for PHA production by activated sludge.

KEYWORDS:

Activated sludge, Aerobic dynamic feeding, Carbon source, Excess sludge fermentation, Polyhydroxyalkanoates

INTRODUCTION

As a fully biodegradable and biocompatible plastic, polyhydroxyalkanoate (PHA) is an interesting alternative to petrochemical derivate plastic due to their similar characteristics (Anderson and Dawes, 1990). PHA are the polyesters that accumulate as intracellular carbon, energy and reducing-power storage material in over 300 various microorganisms (Steinbüchel, 1992). PHA can be biosynthesized from renewable resources, allowing for a sustainable and closed-cycle process for the production and use of such polymers (Braunegg et al., 1998). Currently, PHA synthesis at industrial scale is based on microbial isolates and well defined substrates (Patnaik, 2005). However, the cost of PHA produced thus is still too high for PHA to compete with the conventional plastic commodities. Economic evaluation showed that the production expense of PHA can be reduced over half if renewable waste materials and activated sludge were used (Serafim et al., 2004). Besides, investigation of the process optimization techniques to increase the PHA production efficiency can help to widen the application of PHA. Above all, almost 30% of total PHA production cost is attributed to the carbon source (Salehizadeh and Van Loosdrecht, 2004).

Additionally, a great amount of excess sludge is generated daily worldwide. Handling, treatment and ultimate disposal of the excess sludge account for 40–60% of the total operational cost of an activated sludge treatment plant (Liu, 2003). One strategy for excess sludge management is moving towards reutilization of sludge as useful resources, such as fermenting the excess sludge to generate carbon source for PHA production by pure culture (Lee and Yu, 1997) and for phosphorus removal by activated sludge (Tong and Chen, 2007). Volatile fatty acids (VFAs) is one of the main intermediates in the anaerobic sludge fermentative liquid (Yuan et al., 2006; Tong and Chen, 2007) and the most suitable substrate for PHA storage. Under alkaline conditions, the yield of VFAs was enhanced significantly from excess sludge anaerobic fermentation (Yuan et al., 2006; Chen et al., 2007).

PHA synthesis by activated sludge is possible to reduce PHA production cost, since its sterilization, equipment and control requirements are lower and the microbial communities in activated sludge can adapt well to the complex substrates present in the agroindustrial wastes (Salehizadeh and Van Loosdrecht, 2004). Basic and applied research on this field has been implemented in the past decade (Lemos et al., 2003; Dias et al., 2005, 2006; Dionisi et al., 2006; Serafim et al., 2006, 2007), focusing on areas such as process configuration, reactor operational strategies, process modeling and control, metabolic pathway analysis, microbial characterization and polymer characterization.

Improving the intracellular PHA content is important for decreasing the extraction and recovery cost of PHA downstream processing. The PHA production process known as “feast and famine” or as “aerobic dynamic feeding (ADF)” has a high potential to enhance the intracellular PHA content and specific storage rate of PHA by activated sludge (Serafim et al., 2004; Dias et al., 2005; Dionisi et al., 2006). Since under transient conditions, e.g. insufficiency of an essential growth limiting component or temporary presence of excess carbon source, some bacterial in activated sludge can adapt physiologically to the exposure of high substrate concentration rapidly, uptake substrate quickly and store PHA in a more balanced way (Daigger and Grady, 1982; van Loosdrecht et al., 1997). Periodic substrate feeding aerobically creates an alternation of excess and lack of extra carbon source that will favor the microorganisms most able to store the substrate quickly during the feast phase and then reutilize it for growth during the famine phase (Majone et al., 1999). To reduce the PHA production cost and the disposal amount of excess sludge simultaneously, based on the above considerations, this research investigates the feasibility of PHA production by activated sludge by using VFAs generated from excess sludge fermentation.

Ammonia and phosphorus in the fermentative VFAs are removed under thermophilic and alkaline conditions and by adding magnesium to form struvite deposition. The second one is PHA accumulation by inoculating activated sludge submitted to aerobic transient carbon supply. In the first stage, to provide carbon source for PHA production, the excess sludge having treated municipal wastewater, was fermented under anaerobic, thermophilic and alkaline conditions. Acidogenic fermentation transforms most of biodegradable component in the municipal sludge at high rate into a mixture of VFAs, carbohydrates and proteins. In the second stage, the municipal sludge taken from the secondary sedimentation tank was used immediately and directly to degrade the VFAs-containing fermentative liquid and accumulate PHA, which means the sludge used as inoculation was not domesticated or enriched previously, so as to economize the volume of PHA production reactor. This stage was operated by aerobic periodic feeding in a lab-scale batch reactor.

METHOD

Sludge Source and the Characteristics

The excess sludge used as the raw material to generate VFAs was sampled from the secondary sedimentation tank of a municipal wastewater treatment plant at Shatin in Hong Kong, which was operated with a traditional activated sludge process. The sludge samples were concentrated by settling at 4 °C for 24 h before they were fermented to generate VFAs. The average characteristics of the sludge after settlement are as follows: pH 6.8 ± 0.2 , TSS (total suspended solids) $13\,115 \pm 125$ mg/L, VSS (volatile suspended solids) $9\,901 \pm 65$ mg/L, DOC (dissolved organic carbon) 53 ± 12 mg/L, TOC (total organic carbon) $5\,470 \pm 76$ mg/L, VFAs (as TOC) 9.5 ± 1.8 mg/L, and the analysis was replicated three times for every sludge sample. In the excess sludge samples, proteins and carbohydrates, which account for about $55 \pm 10\%$ of TOC together, are the two predominant organic compounds in excess sludge; the lipid and oil in the excess sludge accounts for around 1% of TOC.

The activated sludge used as the inoculum to produce PHA came from a 15 L lab-scale sequencing biological reactor (SBR) treating real municipal wastewater, which had the influent TOC of 19–55 mg/L, sludge retention time (SRT) of 10 d, and operated aerobically under room temperature (21 ± 1 °C). Before inoculation, the sludge was concentrated by centrifuge at 1000 rpm for 20 min and utilized immediately to accumulate PHA without previous acclimation.

VFAs Generation by Sludge Fermentation under Various pH and Temperature

Batch experiments were conducted under anaerobic conditions to investigate the influence of temperature (21 ± 1 °C, 35 ± 1 °C and 60 ± 1 °C) and pH (pH 8.0, 9.0, 10.0, 11.0 and no pH control as blank) on the optimization yield of VFAs. The operation conditions were summarized in Table 1. In each airtight beaker with working volume of 500 mL, pre-settled excess sludge with 500 mL was added to generate VFAs. The beakers were sparged with nitrogen gas for 30 s to remove oxygen from the headspace, enveloped by aluminium foil, and mixed by magnetic stirrer at 100 rpm. Five beakers were surrounded outside with thermo-resistance wire to set the temperature at 35 ± 1 °C and 60 ± 1 °C, respectively. The temperature was monitored by thermometer inside the reactors to maintain the temperatures consistent. Another five beakers were placed at room temperature (21 ± 1 °C). Every 4 h throughout the experiments, the pH in each beaker was adjusted by adding 3 M NaOH or 3 M HCl to maintain at a certain pH value according to Table 1. A beaker without pH adjustment was used as a blank control. To enhance the VFAs yield, sodium dodecylbenzene sulfonate (SDBS) was added at the dosage of 0.02 g/gVSS in each batch experiments. Since the VFAs yield after SDBS addition is over 7 times of that in

the absence of SDBS (Jiang et al., 2007). SDBS is a widespread used surfactant, which can be easily found in excess activated sludge. The presence of SDBS could strengthen the solubilization of sludge particulate organic-carbon, hydrolysis of solubilized substrate and acidification of hydrolyzed products, and the decrease of methanogenic bacteria activity (Jiang et al., 2007).

Table 1
Batch experiment conditions to generate VFAs from excess sludge fermentation

Batch	Temperature (°C)	pH	Initial excess sludge characteristics (mg/L)
A1	35 ± 1	8.0 ± 0.1	TSS: 13260, VSS: 9845, DOC: 43, TOC: 5395, VFAs (as TOC) 11.5
A2	35 ± 1	9.0 ± 0.1	
A3	35 ± 1	10.0 ± 0.1	
A4	35 ± 1	11.0 ± 0.1	
A5	35 ± 1	No control	
B1	60 ± 1	8.0 ± 0.1	TSS: 13110, VSS: 9878, DOC: 54, TOC: 5461, VFAs (as TOC) 9.3
B2	60 ± 1	9.0 ± 0.1	
B3	60 ± 1	10.0 ± 0.1	
B4	60 ± 1	11.0 ± 0.1	
B5	60 ± 1	No control	
C	21 ± 1	10.0 ± 0.1	TSS: 12990, VSS: 9985, DOC: 63, TOC: 5541, VFAs (as TOC) 7.9

Analytical Methods

Sludge samples from the reactors were immediately filtered through a Whatmann GF/C glass microfiber filter (1.2 µm pore size). The filtrate was immediately analyzed for VFAs, TOC, DOC, SOP, ammonium and pH, and the filter was assayed for PHA, TSS and VSS. The analyses of pH, TSS, and VSS were conducted in accordance with Standard Methods (APHA, 1995). TOC and DOC were measured by Shimadzu TOC-5000A TOC analyzer equipped with ASI-5000A auto sampler. The analyses of PO_3^{4-}P , $\text{NH}_4\text{-N}$, pH, TSS and VSS were conducted in accordance with standard methods (APHA, 1995). Cell dry weight was quantified as the VSS. According to (Yuan et al., 2006), VFAs was analyzed by collecting the filtrate in a 1.5 mL gas chromatography (GC) vial, and 3% H_3PO_4 was added to adjust the pH to approximately 4.0. A HP6890 GC with flame ionization detector (FID) and equipped with a 30m* 0.32 mm *0.25 mm CPWAX52CB column was utilized to analyze the yield and composition of VFAs. Nitrogen was the carrier gas and the flux was 50 mL/min. The injection port and the detector were maintained at 200 °C and 220 °C, respectively. The oven of the GC was programmed to begin at 110 °C and to remain there 2 min, then to increase at a rate of 10 °C/min to 200 °C, and to hold at 200 °C for 2 min. The sample injection volume was 1.0 µL. The total VFAs content was calculated as the sum of measured acetic, propionic, n-butyric, isobutyric, n-valeric, and iso-valeric acid. The standards of these acids were purchased from Sigma (St. Louis, MO, USA).

RESULTS AND DISCUSSION

VFAs Generation at Various pH and Temperature

To optimize the yield of VFAs in the excess sludge fermentative liquid, excess sludge fermentation was conducted in batch reactors at various pH values (8.0, 9.0, 10.0 and 11.0) and at three anaerobic fermentation temperatures (21 ± 1 °C, 35 ± 1 °C and 60 ± 1 °C). Figs. 1 and 2 show the effects of pH, temperature and fermentation time on the VFAs generation from alkaline sludge fermentation. The initial total VFAs was about 0.65 ± 0.30 mgTOC/gVSS. The yield of VFAs was calculated as mg TOC per mg initial VSS, and the initial VSS was 9901 ± 153 mg/L for experiment of A, B and C. It was obvious that during the initial fermentation time, the VFAs concentration at each pH value increased gradually with the rise of pH and temperature, which indicated that more soluble substrates were produced from particulate organics in excess sludge under the alkaline conditions. It might be the result that the excess sludge hydrolysis rate was accelerated under alkaline conditions and at higher temperatures.

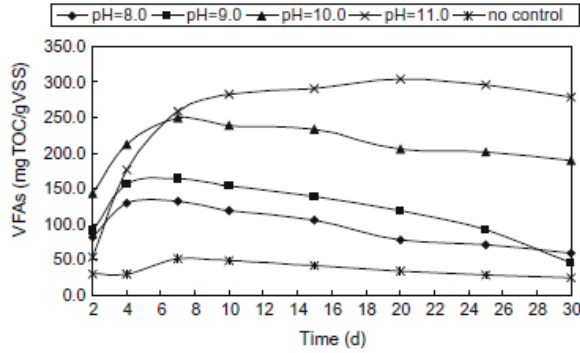


Fig. 1. Effects of pH values and fermentation time on total VFAs production at 60 °C.

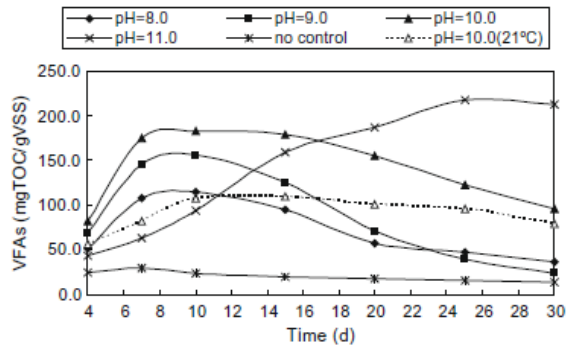


Fig. 2. Effects of pH values and fermentation time on total VFAs production at 35 °C and 21 °C.

Presented as Fig. 1, it was observed that the total VFAs production increased with the increase of fermentation time. It also showed that the total VFAs production on the 7th day linearly increased with pH from pH 8.0 to 10.0 (VFAs = 41.35pH_206.61, $R^2 = 0.96$). Although high VFAs production was achieved at both pH 10.0 and pH 11.0 on the 7th day, stronger alkaline condition resulted in more removal of ammonium from the fermentative liquid, which could improve the intercellular PHA content by activated sludge (this consideration would be explored in the following text). Thus, sludge fermentation conducted at pH 11.0 was preferable. After 7 d, further increasing the fermentation time at pH from 8.0 to 10.0 did not result in the increase of total VFAs production.

Revealed as Fig. 2, during alkaline sludge fermentation at 21 °C and 35 °C, it had the similar VFAs generation trends like that at 60 °C shown in Fig. 1, except for pH 11.0. At pH 10.0, the amount of VFAs generated and consumed in the sludge fermentative liquid at 35 °C was lower than that at 60 °C, but was about twice as large as that at 21 °C. Furthermore, it took 7 d and 10 d, respectively, to obtain the maximum VFAs yield at 35 °C and 21 °C. This could be explained by that higher temperature was more efficient to generate soluble organic compound and VFAs, and could enhance the activity of bacterial communities for hydrolysis, acidification, and methane generation during the anaerobic sludge fermentation. And most methanogenic bacteria with an optimum function could not be maintained in alkaline medium. When the pH increased from 8.0 to 11.0, the methane production was therefore decreased.

Comparing the VFAs yield in Figs. 1 and 2, the results indicate that fermentation temperature also had influence on the yield and productivity of VFAs generation. The different performance of VFAs generation between 35 °C and 60 °C implied that the sludge fermentation at higher temperature has shorter lag-stage for biological adaptation and higher acidification activity during the alkaline sludge fermentation.

These results showed that the production of VFAs could be significantly improved and maintained stable by controlling fermentation pH at 11.0 when anaerobic excess sludge fermentation was conducted at 60 °C and the 7th day, and the optimal yield of VFAs is 258.65 mgTOC/g VSS. Since the initial VSS concentration for fermentation was 9901 mg/L, the concentration of VFAs in the fermentative liquid was 2560.64 mgTOC/L. In the fermentative liquid, acetic and propionic acids were the main products at pH from 10.0 to 11.0, while pH 8.0 and 9.0 favored the production of butyric and valeric acids. Storage yields varied from 0.37 to 0.50 Cmmol - HA/Cmmol VFAs. This performance was also observed when molasses was acidogenic fermented at pH from 5

to 7 that lower PH preferred to producing acetic and propionic acids and higher pH favoured the production of butyric and valeric acids (Albuquerque et al., 2007).

Ammonium and Phosphorus Recovery from Excess Sludge Fermentation Liquid

Phosphorus recovery and further ammonium removal from the fermentative liquid of excess sludge was implemented by adding Mg^{2+} to the fermentative liquid to form the precipitation of struvite at 21 °C. Results show that the phosphorus recovery efficiency increased with pH from 8.0 to 11.0, there was no significant increase after pH 10.5 and the phosphorus recovery rate was 93.0% at pH 10.5. So the suitable pH for phosphorus recovery was controlled at pH 10.5. As the formation of struvite consumed ammonium, the removal of ammonium was also observed and increased with pH from 8.0 to 10.5. When pH value was higher than pH 10.5, due to the volatilization of ammonium while mixing, there was still some ammonium removal.

The organic compounds concentration in the fermentative liquid has an influence on phosphorus and ammonium recovery (Tong and Chen, 2007). With the increase of Mg/SOP dosage from 1.2 to 3.0 mol/mol, both phosphorus and ammonium recovery increased, but further increasing Mg/SOP to 2.6 resulted in only marginal improvement of both phosphorus and ammonium recovery, which indicated that Mg/SOP should be maintained at 2.6/1. The theoretical value of the Mg/SOP molar ratio is 1/1 when MAP is formed. The possible reason was that some of the Mg combined or even co-precipitated with the solvable proteins and lipids, which was interpreted from the data in Table 2 that some TOC was removed during phosphorus recovery. In fact, at a fixed Mg/SOP molar ratio of 2.6/1, when the fermentative liquid concentration was 0%, 25%, 50%, 75%, and 100%, the SOP removal was 99.8%, 97.6%, 96.2%, 93.7%, and 91.5%, respectively, which suggested that with the increase of organic compounds, the SOP removal decreased, and more Mg should be added if a higher SOP removal was required.

At Mg/SOP = 2.6/1 and pH 10.5, the removal efficiency of SOP and ammonium increased rapidly to 94.5%, and 35.0%, respectively and no obvious increase after 2 min of reaction. At other Mg/SOP ratios, the same observation could be made. It seems that 2 min was enough for efficient ammonium recovery.

Table 2 summarizes the variations in the main composition of the fermentative liquid after struvite precipitation under conditions of 21 °C, pH 10.5, Mg/SOP = 2.6 mol/mol, and a reaction time of 2 min. Along with the removal of phosphorus and ammonium, there were some DOC and VFAs removed from the fermentative liquid. Also, it can be calculated from Table 2 that after ammonium recovery, the VFAs accounted for 36.6% of the DOC and the VFAs were composed of 80.5% acetic, 11.4% propionic, 2.2% iso-valeric, 1.3% iso-butyric, 4.0% n-butyric, and 0.6% n-valeric acid. In the literature, it was also found that the acetic acid was the most prevalent product in the fermentative VFAs at any fermentation time and any pH value under alkaline conditions during the anaerobic

fermentation of excess sludge (Yuan et al., 2006; Chen et al., 2007). The reason for the high ratio of acetic acid to other VFAs is explained as follows. Protein and carbohydrate content was about 55% in the excess sludge of this study. More soluble protein and carbohydrate were acidified to produce more VFAs under alkaline conditions and at higher fermentation temperature. Hydrolysis and acidification of protein and carbohydrate contributed to the generation of VFAs with 2–5 carbon chain. Propionic, iso-butyric, n-butyric, iso-valeric, or n-valeric acids were easily biodegraded to form acetic acid and were not much accumulated in the anaerobic fermentation system. Methanogens had little activity under alkaline conditions and cannot utilize acetic acid, which has also been observed by other researchers (Cai et al., 2004; Yuan et al., 2006). Higher might enhance the bacterial activity of hydrolysis so as to lead to more yield of VFAs.

Table 2
Variations of fermentative liquid during phosphorus and ammonium recovery at 60 °C, 7 d and pH 11.0

	SOP	NH_4^+-N	DOC	DOC: NH_4^+ :SOP	VFAs ^a
Before recovery (mg/L)	121.6	193.5	7425	61.1:1.6:1	2560.64
After recovery (mg/L)	10.4	71.5	6877	661.3:6.9:1	2437.55
Removal efficiency (%)	91.5	63.0	7.4	–	4.8

^a Unit of VFAs is mg DOC/L.

Production of PHA Fed by VFAs-Containing Fermentative Liquid

The aim of feeding fermentative VFAs by pulses was to enhance the PHA storage capacity of the cells and to avoid the inhibition from feeding the same amount of substrates by one pulse. Clarified fermentative liquid generated at 60 °C, fermentation time of 7 d and pH 11.0 was used as substrates. Fermentative liquid with 1830 mL containing 2437.55 mg TOC/L of VFAs was split equally and supplied in three pulses. This feeding regimen resulted in the decrease of each initial organic load rate (OLR) of the three feeding pulses. The initial VSS of the excess sludge was 2045 mg/L and the concentration ratio of VFAs to ammonium was 34 mg/mg (TOC:NH₄ – N). The exact time to add a new pulse of VFAs-containing fermentative liquid was determined by the sudden increase in DO concentration caused by substrate exhaustion. Typical results of VFAs uptake, ammonium consumption, biomass growth and PHA accumulation during the batch experiment under ADF conditions are shown in Fig. 3.

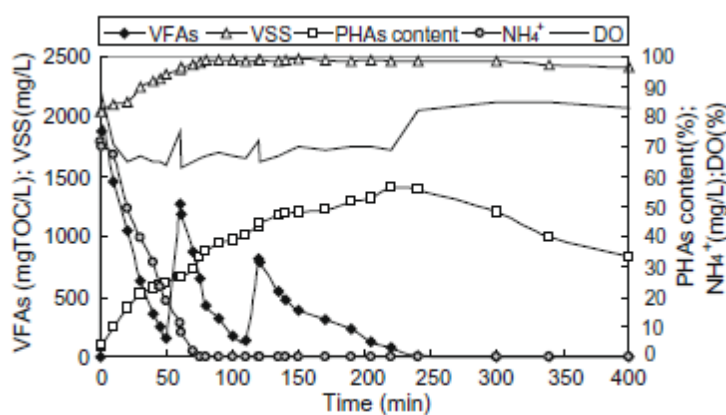


Fig. 3. Evolution of VFAs, PHA, ammonium, cell growth and DO during a batch run.

The biomass taken from the municipal wastewater treatment system was inoculated into batch reactor operating as ADF process. The sludge accumulated PHA immediately and the intercellular PHA content increased from the initial 3.5% to 26.7% before the second substrate feeding, which indicated that the sludge showed a quick adaptation to the new conditions. Splitting the substrate in three pulses led to the cell PHA content of 56.5% at the time of the total VFAs depletion, which took 3 h and 40 min. This was a high value of PHA content obtained by using real wastes as carbon source and activated sludge as inoculation without sludge acclimation. The fourth feed of fermentative VFAs with the same amount of the third feed did not lead to further increase of intracellular PHA content and the carbon source conversion rate is just 23% comparing with that value in the third feed (data is not shown here). This observation implies that the PHA accumulation capacity by excess sludge is almost exhausted. Fermentative VFAs was quickly taken up and stored as PHA. The quick adaptation of excess sludge to the transient substrate feeding might be because of the high fraction of acetic acid in the fermentative VFAs and the proper substrate concentration not to inhibit the activity of bacterial communities in activated sludge. Acetic acid is the favorite carbon source for activated sludge to synthesize PHA.

Ammonia began to be consumed 10 min after the feeding of fermentative VFAs. It might be because cell growth needs time to adapt their cellular composition (e.g. proteins, RNA, DNA) physiologically to the transient presence of extra substrate (Majone et al., 1999). Ammonia was consumed while substrate was taken up in the “feast” phase, indicating that cell growth and PHA accumulation occurred simultaneously. PHA production and carbon source consumption were linear during almost all of the “feast” period. Ammonia was exhausted within the first one hour, which means the beginning of the “famine” period. The cell growth decreased significantly when the ammonia became limiting and the carbon source taken up was used mainly to accumulate PHA. This phenomena were also observed by Serafim et al. (2004). In the “fam-ine” phase, PHA was mainly used for cell maintenance. Cell growth on PHA did not occur in the “famine” phase, since the hydrolysis of intracellular proteins releasing ammonia during a batch experiment could be ignored.

The DO decreases immediately after substrate addition, remaining almost constant during the “feast” period and rising again after the carbon source exhaustion. Theory was in agreement with the variations of DO concentration (data were not shown). These results clearly indicate that the amount of substrate consumed during the “feast” period was used for PHB storage, cell growth, and maintenance processes. The global fraction of PHA content increased through degrading VFAs at the end of the each feeding pulse was 0.33, 0.38 and 0.39 mg/mg, respectively. Such high yield of PHA and quick adaptation of activated sludge to the fermentative VFAs implied that supplying a high substrate concentration by pulses stimulated the storage of PHA. Since the available ammonium was depleted before the pulse of the second feeding, the amount of VFAs used for growth was always low compared with the one used for polymer storage. The specific PHA storage rate

of the three fermentative liquid pulse was 0.33, 0.38 and 0.23 mg HAs/mg VSS h, respectively, which were similar to those obtained with high substrate dosage (Beun et al., 2000; Serafim et al., 2004), but were one order of magnitude higher than those achieved by pure cultures like *Ralstonia eutropha* (0.019 mg HAs/mg VSS h) (Kim et al., 1994), *Alcaligenes latus* (0.031 mg HAs/mg VSS h) (Yamane et al., 1996) or recombinant *Escherichia coli* (0.042 mg HAs/mg VSS h) (Lee et al., 1994). In this feast and famine process, comparing with pure cultures, activated sludge could possess the same volumetric productivities of PHA with much less cell concentration, which results in smaller aeration requirements. That the storage rate in the second pulse was higher than the first one was because of the depletion of ammonium, resulting in more carbon available for the storage process. That the storage rate decreased from the second to the third pulse was confirmed by the decrease in the substrate consumption rate observed for the third pulse. The average observed yield of biomass was 0.124 mg/mg, and the maximum VSS was 2473 mg/L. When the external VFAs were excess and ammonium was present, the main uptake was driven into PHA storage and the lesser fraction was transformed into the biomass. Biomass growth was ceased under ammonium limitation, which was approved by the fact that no VSS increase after the 70th minutes of the batch reaction.

Table 3
PHA content and PHA production rate achieved by activated sludge

Process	Substrate	PHA	PHA content (%)	PHA production rate (mgTOC/gTSS/h)
Anaerobic-aerobic (without sludge acclimation)	Municipal wastewater + acetic acid	PHB	30	28
ADF (with sludge acclimation)	acetic acid	PHB	78.5	320
ADF (without sludge acclimation)	Fermentative VFAs	HB:HV (88.1:11.9)	56.5	310

In Table 3, the PHA content and PHA production rate achieved by activated sludge in this study is compared to the one obtained by other researchers. Results show that the excess sludge without sludge acclimation feeding by fermentative VFAs could also accumulate PHA quickly with acceptable intracellular PHA content. The acetate acid and propionic acid in the fermentative VFAs was 80.5% and 11.4% (mol%), respectively, the composition of PHA produced was the mixture of HB and HV monomer. The HB monomer in the PHA was 88.1% (mol%). It is because that the composition of PHA produced would be influenced by the composition of carbon source (Lemos et al., 2006).

CONCLUSION

Higher temperature and alkaline condition were the favorite conditions to enhance the VFAs yield and ammonium removal from excess sludge fermentation. The major acids in the fermentative VFAs were acetic acid. The released phosphorus and residual ammonium was recovered by formation of struvite precipitation. The maximum PHA content accounted for 56.5% of the dry cell, which was a high value of PHAs content obtained by using real wastes as carbon source and municipal sludge without acclimation as inoculation. VFAs generated from excess sludge fermentation were a suitable carbon source for PHAs production by activated sludge.

ACKNOWLEDGEMENTS

The authors wish to express their sincere gratitude to the Research Grant from The Hong Kong Government Research Grant Council (PolyU 5159/09E), The Hong Kong Polytechnic University for the support of this research.

REFERENCES

- Albuquerque, M.G.E., Eiroa, M., Torres, C., Nunes, B.R., Reis, M.A.M., 2007. Strategies for the development of a side stream process for polyhydroxyalkanoate (PHA) production from sugar cane molasses. *Journal of Biotechnology* 130 (4), 411–421.
- Beun, J.J., Paletta, F., Van Loosdrecht, M.C.M., Heijnen, J.J., 2000. Stoichiometry and kinetics of poly-beta-hydroxybutyrate metabolism in aerobic, slow growing, activated sludge cultures. *Biotechnology and Bioengineering* 67 (4), 379–389.

- Cai, M., Liu, J., Wei, Y., 2004. Enhanced biohydrogen production from sewage sludge with alkaline pretreatment. *Environmental Science and Technology* 38 (11), 3195–3202.
- Chen, Y., Jiang, S., Yuan, H., Zhou, Q., Gu, G., 2007. Hydrolysis and acidification of waste activated sludge at different pHs. *Water Research* 41 (3), 683–689.
- Chua, A.S.M., Takabatake, H., Satoh, H., Mino, T., 2003. Production of polyhydroxyalkanoates (PHA) by activated sludge treating municipal wastewater: effect of pH, sludge retention time (SRT), and acetate concentration in influent. *Water Research* 37 (15), 3602–3611.
- Dias, J.M.L., Lemos, P.C., Serafim, L.S., Oliveira, C., Eiroa, M., Albuquerque, M.G.E., Ramos, A.M., Oliveira, R., Reis, M.A.M., 2006. Recent advances in polyhydroxyalkanoate production by mixed aerobic cultures: from the substrate to the final product. *Macromolecular Bioscience* 6 (11), 885–906.
- Dias, J.M.L., Serafim, L.S., Lemos, P.C., Reis, M.A.M., Oliveira, R., 2005. Mathematical
- Din, M.F.M., Ujang, Z., van Loosdrecht, M.C.M., Ahmad, A., Sairan, M.F., 2006. Optimization of nitrogen and phosphorus limitation for better biodegradable plastic production and organic removal using single fed-batch mixed cultures and renewable resources. *Water Science and Technology* 53 (6), 15–20.
- Dionisi, D., Majone, M., Vallini, G., Di Gregorio, S., Beccari, M., 2006. Effect of the applied organic load rate on biodegradable polymer production by mixed microbial cultures in a sequencing batch reactor. *Biotechnology and Bioengineering* 93 (1), 76–88.
- Lee, S., Yu, J., 1997. Production of biodegradable thermoplastics from municipal sludge by a two-stage bioprocess. *Resources, Conservation and Recycling* 19 (3), 151–164.
- Lemos, P.C., Serafim, L.S., Reis, M.A.M., 2006. Synthesis of polyhydroxyalkanoates from different short-chain fatty acids by mixed cultures submitted to aerobic dynamic feeding. *Journal of Biotechnology* 122 (2), 226–238.
- Lemos, P.C., Serafim, L.S., Santos, M.M., Reis, M.A.M., Santos, H., 2003. Metabolic pathway for propionate utilization by phosphorus-accumulating organisms in activated sludge: C-13 labeling and in vivo nuclear magnetic resonance. *Applied and Environmental Microbiology* 69 (1), 241–251.
- Liu, Y., 2003. Chemically reduced excess sludge production in the activated sludge process. *Chemosphere* 50, 1–7.
- Ma, C.K., Chua, H., Yu, P.H.F., Hong, K., 2000. Optimal production of polyhydroxyalkanoates in activated sludge biomass. *Applied Biochemistry and Biotechnology* 84–86, 981–989.
- Patnaik, P.R., 2005. Perspectives in the modeling and optimization of PHB production by pure and mixed cultures. *Critical Reviews in Biotechnology* 25 (3), 153–171.
- Salehizadeh, H., Van Loosdrecht, M.C.M., 2004. Production of polyhydroxyalkanoates by mixed culture: recent trends and biotechnological importance. *Biotechnology Advances* 22 (3), 261–279.
- Serafim, L.S., Lemos, P.C., Oliveira, R., Reis, M.A.M., 2004. Optimization of polyhydroxybutyrate production by mixed cultures submitted to aerobic dynamic feeding conditions. *Biotechnology and Bioengineering* 87 (2), 145–160.
- Serafim, L.S., Lemos, P.C., Rossetti, S., Levantesi, C., Tandoi, V., Reis, M.A.M., 2006. Microbial community analysis with a high PHA storage capacity. *Water Science and Technology* 54 (1), 183–188.
- Serafim, L.S., Lemos, P.C., Torres, C., Reis, M.A., Ramos, A.M., 2007. The influence of process parameters on the characteristics of polyhydroxyalkanoates produced by mixed cultures. *Macromolecular Bioscience*. doi:10.1002/mabi.200700200.
- Steinbüchel, A., 1992. Biodegradable plastics. *Current Opinion of Biotechnology* 3, 291–297.
- Tong, J., Chen, Y., 2007. Enhanced biological phosphorus removal driven by shortchain fatty acids produced from waste activated sludge alkaline fermentation. *Environmental Science and Technology* 41 (20), 7126–7130.
- Wang, Y.J., Hua, F.L., Tsang, Y.F., Chan, S.Y., Sin, S.N., Chua, H., Yu, P.H.F., Ren, N.Q., 2007. Synthesis of PHAs from waster under various C: N ratios. *Bioresource Technology* 98 (8), 1690–1693.
- Yuan, H., Chen, Y., Zhang, H., Jiang, S., Zhou, Q., Gu, G., 2006. Improved bioproduction of short-chain fatty acids (SCFAs) from excess sludge under alkaline conditions. *Environmental Science and Technology* 40 (6), 2025–2029.

Structural Engineering

FINITE ELEMENT ANALYSIS OF FRP WRAPS IN SPLIT-DISK TESTS

S. Q. Li, J. F. Chen and L. A. Bisby
Institute for Infrastructure and Environment
Joint Research Institute for Civil and Environmental Engineering
School of Engineering, The University of Edinburgh
Edinburgh EH9 3JL, Scotland, U.K. E-mail: J.F.Chen@ed.ac.uk

ABSTRACT

The strengthening of concrete by applying bonded fiber-reinforced polymer (FRP) jackets has become a popular retrofit technique. Failure of such FRP-wrapped columns is usually governed by rupture of the FRP in the hoop direction. Two common material tests have been used to obtain the hoop strength and rupture strain of FRP composites used in these applications: tensile tests of flat coupons and so-called split-disk tests. The FRP rupture strain obtained from a split-disk test is usually lower than that obtained from a flat coupon test, but there is neither a well-defined relationship between the two results nor a comprehensive explanation for why they should have different values. This paper presents a finite element (FE) analysis of the FRP hoop strains in the split-disk test. The results show that the local strains in an FRP ring in a split-disk test are increased by the geometric discontinuities at the ends of the FRP and circumferential bending of the FRP ring at the gap arisen from the relative moment of the two half disks. The model predicts that the FRP will rupture once the strain at one of the above locations reaches the FRP rupture strain, leading to a lower apparent tensile strength than that obtained from flat coupon tests.

KEYWORDS

Finite element analysis, fibre reinforced polymers, FRP strengthening, tensile strength, split-disk test.

INTRODUCTION

Failure of a circular, fiber reinforced polymer (FRP) wrapped concrete is usually governed by rupture of the FRP in the hoop direction, and the designer consequently needs to know the strain or stress at which rupture of the FRP wrap will occur (Teng and Lam 2004). The tensile rupture of FRP occurs in FRP wrapped columns when the hoop strain in the FRP reaches 58 to 91% of its ultimate tensile strength (Lam and Teng 2004), which is typically determined from flat coupon tests (ASTM 1995) or split-disk tests (ASTM 1992) as shown in Figure 1, or sometimes from the FRP properties supplied by the FRP manufacturer (Lam and Teng 2002). This large scatter of FRP failure strain gives rise of large uncertainties in design.

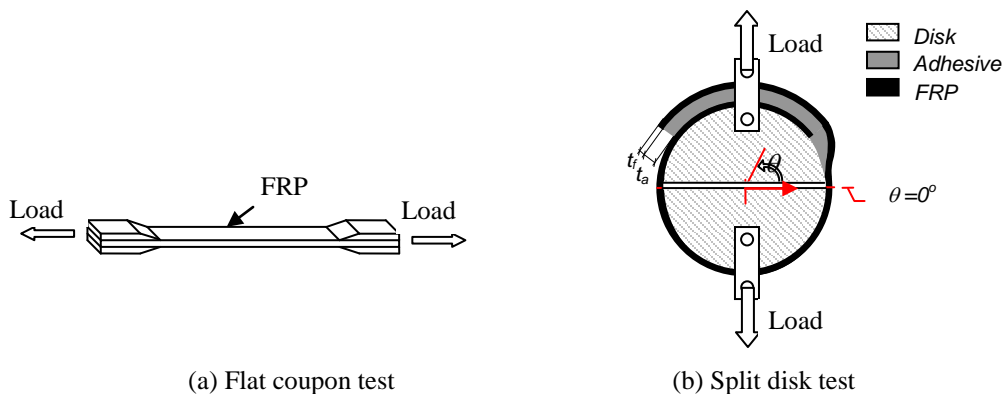


Figure 1. FRP strength test methods

Numerous experiments have shown that the FRP rupture strain determined from the split-disk test is significantly lower than that determined from the tensile coupon test or from the manufacturer (Lam and Teng, 2004; Mirmiran and Shahawy, 1997; Tamuzs et al., 2006). A careful study of GFRP tube properties was conducted by Mirmiran and Shahawy (1997), in which micro-mechanics equations and rules of mixture were used to determine the analytical strength and elastic modulus of FRP tubes. Split-disk tests were also reported, and the results showed that the strength and elastic modulus obtained from the analytical approach were higher than those obtained from the split-disk method (Mirmiran, 1996). Both flat coupon and split-disk tests of FRP wraps were presented by Lam and Teng (2004). This was the first paper to present a methodical experimental investigation into the different contributory causes, concluding that there are at least two contributing factors to which the reduction of ultimate strains of FRP in split-disk tests may be due, namely: a) curvature of the FRP, reducing its strain capacity; and b) circumferential bending of the FRP ring at the gap created by the relative moment of the two half disks. Three kinds of CFRP wrap split-disk specimens were tested by Tamuzs et al. (2006). The results showed that the ultimate strains obtained from tests were considerably lower than the technical data given by the manufacturer.

This paper presents a finite element (FE) analysis of the split-disk test for FRP composites. Comparisons between the predictions of the model and test results are given to demonstrate the validity of the FE approach and to numerically quantify the reduction of the FRP rupture strain.

GEOMETRY AND MATERIALS

Geometry

Two assembled half disks with FRP wrap are considered. Figure 1(b) shows such disks with one layer of FRP wrapped around their circumference. The disks have a radius R , and are wrapped with an FRP sheet of thickness t_f . There is an adhesive layer of uniform thickness t_a between the FRP and the disks and between the FRP wraps in the overlapping (splice) region. A polar coordinate system is used to describe position (Fig. 1b) using a circumferential angle, θ . The FRP starts at $\theta = 90^\circ - \alpha/2$ at the inner free end of the wrap and finishes at $\theta = 450^\circ + \alpha/2$ at the outer free end, giving an overlap zone of angular length α .

The change in FRP wrap radius necessary for the outer layer of FRP to overlap the inner layer occurs within a transition zone of angular length β . The shape of the transition is assumed to be sinusoidal. Reference values of $R = 75\text{mm}$, $\alpha = 114.6^\circ$ (which are the dimensions of specimens tested by Lam and Teng (2004)), and $\beta = 30^\circ$ are used in the paper.

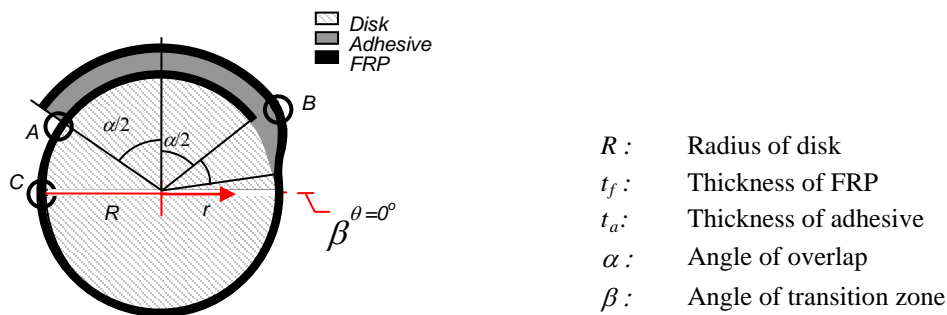


Figure 2. Geometry of split disk test

It should be noted that such a system contains three important interfaces (Fig. 2): (a) between the disks and the FRP; (b) between the inner surface of the FRP and the adhesive in the transition zone; and (c) between the outer surface of the FRP and the adhesive in the transition zone. For such a system under split-disk tension, stress concentrations are expected to occur on the outer surfaces of the layer of FRP at $\theta = \alpha/2 + 90^\circ$, adjacent to the end of the outmost FRP layer (Location A in Fig. 2) and on the inner surfaces of the layer of the FRP at $\theta = 360^\circ$, adjacent to the end of the innermost FRP layer (Location B in Fig. 2). Furthermore, local bending is expected to occur in the FRP near to the gap created by the relative movement of the two half disks (Location C in Fig. 2).

Properties of the Adhesive

Modern adhesives, particularly those such as the rubber-modified epoxies that are used in FRP strengthening applications with steel or concrete, have a relatively large plastic strain to failure. Therefore, the adhesives' plasticity must be properly included in any analysis to simulate the strain distributions in the system when the adhesive yields. However, material nonlinearity due to plastic behaviour is not often included in the analysis of adhesively bonded joints because of the increased complexity of the mathematical formulation (da Silva et al., 2009). In the current case, comparison of linear and nonlinear material properties was performed and is presented in the paper. An elastic-plastic shear stress model of the adhesive was chosen in the current analysis, in which the yield stress and the failure stress are assumed equal. The adhesive was treated as an isotropic material (Adams and Wake, 1984), described by a bilinear stress-strain curve, and using the von Mises yield criteria coupled with an isotropic work hardening assumption.

The adhesive properties were not examined in previous work on this subject by Lam and Teng (2004) or Tamuzs et al. (2006). The elastic modulus and Poisson's ratio of both the matrix and the adhesive used in the current study were chosen as 3,000 MPa and 0.35 (Dean and Crocker, 2001). A yield strength of 30 MPa was initially used to generate numerical results.

Properties of the FRP Composite

FRP composites are orthotropic materials. The mechanical properties of the composite depend upon the fibre architecture (orientation and distribution) and the relative proportions of the two components (fibre and matrix). The macro properties of a composite may be estimated from the fibre architecture and fibre volume fraction using the laws of mixtures (Vinson and Sierakowski, 2002).

The adhesive properties used in the analysis are given above. Thus, the FRP's properties can be deduced from the fibre, adhesive properties and fibre volume ratio. The resulting properties used in this paper are listed in Table 2.

FINITE ELEMENT MODELLING

The commercial finite element analysis package ANSYS Version 11.0 (2007) was used in the current study. To reduce the computational effort, the split-disk test was modelled as a plane stress problem using the eight-node planar element. The ultimate failure load applied in the FE model was the ultimate strength times the cross-sectional area of the FRP ring.

The two steel half disks which are used to support the sample during testing were considered as rigid bodies and modelled as rigid boundaries in the analysis, the FRP inner surface was defined as a deformable boundary, which was assumed to be in contact with the disks. Surface-to-surface contact elements were applied on these two surfaces, with target elements in the disk surface and contact elements in the FRP surface.

The split of the disks was defined as a displacement of the disk surface. Each rigid disk surface was associated with a "pilot node", whose motion governed the motion of the entire target surface (Ansys, 2007).

Unless mentioned otherwise, the contact surfaces were treated as having zero friction because in a real split-disk test lubricants are usually applied between the FRP ring and the disks to reduce friction. Fig. 3 shows the predicted distributions of FRP hoop strains on the inner and outer surfaces of the FRP in specimen Lam-1 (Lam and Teng, 2004). The diameter of the disks was 150mm and the nominal width of the CFRP ring was 25mm, with an overlap length of 150mm. Additional details of this test can be found in Table 1. This figure shows that stress concentrations occur in three locations in the FRP layers: (a) on the outer surface of the inner layer of FRP adjacent to the outer end of the wrap (Location A) (Fig. 3a); (b) on the inner surface of the outer layer of FRP adjacent to the inner end of the wrap (Location B) (Fig. 3b); and (c) On the inner surface of the inner layer near to the gap created by the relative movement of the two half disks (Location C) (Fig. 3c). These three locations are marked in Fig. 2. The strain value at the two gaps created by the relative movement of the two half disks is essentially the same due to the near symmetry of the disks, and therefore only one gap as shown in Fig. 2 is examined as Location C in this paper.

There are two main types of processes for strengthening concrete using FRPs, one is the use of an adhesively bonded prefabricated plate, and the other is a wet lay-up process. In the former case, the plate and the bonding adhesive layer can be clearly separated, although the exact thickness of the adhesive layer is difficult to control

or define precisely. In the latter case, which is actually the more widely used method for concrete confinement applications, the FRP sheet is formed from the impregnation of the fibres with resin (Teng et al., 2002). Therefore, in the FE modelling of prefabricated wraps, a wrap with nominal thickness should be considered. In the model of a wet lay-up FRP wrap, two options can be used: (a) a similar situation as a prefabricated wrap, with a well-defined adhesive layer; and (b) a wrap with its thickness being equal to the actual thickness of the laminate including the adhesive, with the fibres assumed to be evenly distributed across the plate thickness. Thus, in Option (b), the modulus of elasticity of the FRP wrap times the FRP thickness remains the same as that of Option (a). In the current study, Option (b) is considered.

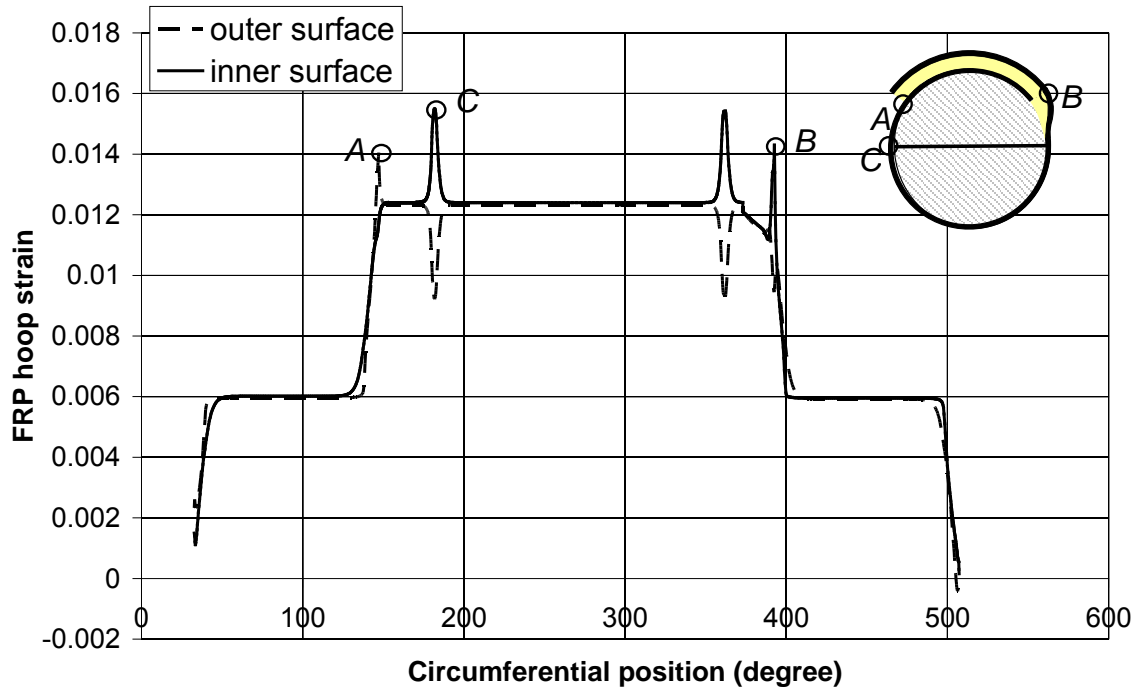


Figure 3. Distribution of FRP hoop strain on the inner and outer surface of FRP

VERIFICATION OF THE FE MODEL AGAINST TEST RESULTS

Test data

A number of specimens were collected from the literature (Table 1). These specimens were simulated with the FE model presented above. The material properties of the FRP composites calculated using rules of mixtures (Vinson and Sierakowski, 2002) are listed in Table 2.

For Lam and Teng's (2004) test specimens, the elastic moduli obtained by them from flat coupon tests used in the FE model because the elastic modulus obtained from split-disk test are less reliable due to factors such as the existence of the overlapping zone. Furthermore, the ultimate strains resulting from the tests were the FRP ultimate strength divided by elastic modulus of the FRP, since the strain gauges are less reliable when they are located at the gap created by the relative movement of the two half disks (Lam and Teng, 2004). The load in the FE model was applied up to the maximum test load in the specimens reported in Tamuzs et al. (2006). Tamuzs et al. (2006) did not report flat coupon tests, so the data provided by the supplier were adopted for Tamuzs-1 to Tamuzs-3 in Table 3.

The actual FRP thicknesses for the specimens report in Tamuzs et al. (2006) are not available. In the FE analysis, the actual thickness of the CFRP measured by Lam and Teng (2004) was used as the nominal thickness for the CFRP in these specimens since the two studies are similar. Also, since the adhesive properties were not reported in Tamuzs et al. (2006), three different adhesive material properties were adopted to examine the FRP hoop strains: linear elastic, linear elastic perfectly plastic with a yield strength of 30MPa and 60 MPa respectively.

Table 1. Details of split disk test specimens

No.	Specimen name	FRP type	Nominal thickness (mm)	Actual thickness (mm)	Number of layers	Width (mm)	Length of overlap (mm)	Diameter (mm)	Elastic modulus (GPa)
1	Lam-1	CFRP	0.165	1.20	1	25	150	150	258.810
2	Lam-2	GFRP	1.27	1.24	1	23	150	150	22.455
3	Tamuzs-1	CFRP	0.17	1.20*	1	20	150	150	200.5
4	Tamuzs-2	CFRP	0.17	1.20*	2	20	150	150	230.5
5	Tamuzs-3	CFRP	0.17	1.20*	3	20	150	150	236

Source of data: Specimens No. 1 and 2 are from Lam and Teng (2004); Specimens No. 3-5 from Tamuzs et al. (2006).

* Estimated value as this data was not reported in the source paper.

Table 2. Properties of FRP constituents and composites

Fibre properties			Fiber volume ratio	Derived properties of FRP composites				
Specimen name	E_f (GPa)	ν_f		E_{11} (GPa)	$E_{22} = E_{33}$ (GPa)	$G_{12} = G_{13}$ (GPa)	G_{23} (GPa)	$\nu_{12} = \nu_{13} = \nu_{23}$
Lam-1	258.81	0.2	13.75%	35.59	3.71	1.46	1.39	0.33
Lam-2	22.46	0.2	60%	22.46	7.72	3.59	3.20	0.26
Tamuzs-1	182.3	0.2	14.17%	28.40	3.69	1.47	1.41	0.33
Tamuzs-2	212.2	0.2	14.17%	32.65	3.70	1.47	1.41	0.33
Tamuzs-3	217.8	0.2	14.17%	33.43	3.70	1.47	1.41	0.33

Note: (a) Direction 1 is the fibre direction, directions 2 and 3 are perpendicular to the fibre direction;

(b) Other Poisson's ratios can be derived from $E_i/E_j = \nu_{ij}/\nu_{ji}$, where $i, j = 1, 2, 3$.

Table 3. Test ultimate strain versus FEA prediction maximum strain

Specimen name	Test			FEA prediction				
	Split disk (%)	Flat coupon or supplier (%)	Reduction factor	Outside overlap zone (%)	In Location A (%)	In Location B (%)	In Location C (%)	Reduction factor
	(1)	(2)	(3)=(1)/(2)	(4)	(5)	(6)	(7)	(8)=(4)/(2)
Adhesive yield strength = 30 MPa								
Lam-1	1.170	1.511	0.77	1.232	1.453	1.478	1.545	0.80
Lam-2	1.902	2.325	0.82	1.991	2.112	2.313	2.520	0.79
Tamuzs-1	0.95	1.92	0.49	0.977	1.241	1.134	1.253	0.78
Tamuzs-2	1.04	1.92	0.54	1.068	1.343	1.341	1.465	0.73
Tamuzs-3	1.13	1.92	0.59	1.163	1.474	1.470	1.673	0.70
Adhesive yield strength = 60 MPa								
Tamuzs-1	0.95	1.92	0.49	0.977	1.595	1.0157	1.250	0.61
Tamuzs-2	1.04	1.92	0.54	1.067	1.697	1.335	1.462	0.63
Tamuzs-3	1.13	1.92	0.59	1.162	1.837	1.605	1.670	0.63
Elastic adhesive property								
Tamuzs-1	0.95	1.92	0.49	0.977	1.926	1.020	1.250	0.51
Tamuzs-2	1.04	1.92	0.54	1.067	2.367	1.334	1.462	0.45
Tamuzs-3	1.13	1.92	0.59	1.162	2.639	1.601	1.670	0.44

Comparison with the Test Results

The results for Lam and Teng's (2004) specimens are discussed here first because complete test data are available for these tests so firm conclusions may be drawn up. The maximum FRP hoop strains predicted by the FE model at the test failure load are compared with ultimate strain from the flat coupon test or provided by the manufacturer in Table 3. Outside the overlapping zone, there is clearly a close agreement between the predicted hoop strain at the failure load (Column (4) in Table 3) and the ultimate strain obtained from the split-disk test (column (1) in Table 3), with a difference generally less than 5%. However, both values are significantly smaller than the flat coupon tensile test results (Column (2) in Table 3), with the strain reduction factors listed in

Columns (3) and (8) respectively in the same table. Therefore, the FE model described above can accurately predict the behaviour of the split-disk test.

For the four FRP hoop strains in the FE results, the maximum strains in Locations A, B and C are significantly larger than the strain remote from these three locations. Furthermore, the maximum strains among these locations are very close to the ultimate tensile strain of the FRP obtained from flat coupon tensile test. Therefore, it can be concluded that in the split-disk test the FRP ruptures once one of the peak strains at locations A, B, or C reaches the FRP flat coupon rupture strain. This leads to a much lower apparent tensile strength than that determined from the flat coupon test.

For the specimens reported by Tamuzs et al. (2006), the predicted strain reduction factor reduces as the yield strength increases. The test reduction factors are smaller than the FE predictions if the adhesive had a yield strength of 30 MPa and 60 MPa but slightly larger if the adhesive is linear elastic. It shall be noted, however, there are other factors such as the Young's modulus and thickness of the adhesive layer as well as the geometrical details at the two ends of the FRP can also affect the strain distribution and thus the strain reduction factor.

CONCLUSIONS

This paper has presented a finite element investigation into the FRP behaviour in a split disk test. In the model, the FRP composite was considered as an orthotropic material, while the adhesive was treated as an elastic-perfectly plastic material. The FE predictions are in close agreement with the test result.

The FE results have shown that there are severe strain concentrations in the FRP at both ends of the FRP wrap and at the position where the two half disks meet. The FRP ruptures when the maximum strain at one of these locations reaches the ultimate tensile strain of the FRP obtained from the flat coupon tensile test. The FRP strain away from these locations is significantly smaller at failure. This explains why the measured ultimate FRP strain in the split-disk test is lower than the rupture strain obtained from the flat coupon test.

ACKNOWLEDGMENTS

The authors would like to thank The China Scholarship Council and the University of Edinburgh for providing S.Q. Li a China/University of Edinburgh Joint Scholarship. The authors would also like to acknowledge the support from the UKIERI (UK India Education and Research Initiative) project (IND/CONT/07-08/E/133) funded by the British Council, the UK Department for Innovation, Universities and Skills (DIUS), Office of Science and Innovation, the FCO, Department of Science and technology, Government of India, The Scottish government, Northern Ireland, Wales, GSK, BL, Shell and BAE for the benefit of the India Higher Education Section and the UK Higher Education Sector. The views expressed are not necessarily those of the funding bodies.

REFERENCES

- Adams, R. D., and Wake, W. C. (1984). *Structural Adhesive Joints in Engineering*, Elsevier Applied Science Publishers.
- Ansys. (2007). "Release 11.0 documentation For ANSYS." Ansys, I. N. C., Canonsburgh, PA.
- ASTM. (1992). "Standard test method for apparent tensile strength of ring or tubular plastics and reinforced plastics by split disk method." *D 2290-92*, West Conshohocken, Pa.
- ASTM. (1995). "Standard test method for tensile properties of polymer matrix composite materials." *D 3039/D 3039M*, West Conshohocken.
- da Silva, L. F. M., das Neves, P. J. C., Adams, R. D., and Speltz, J. K. (2009). "Analytical models of adhesively bonded joints--Part I: Literature survey." *International Journal of Adhesion and Adhesives*, 29(3), 319-330.
- Dean, G. D., and Crocker, L. E. (2001). "The use of finite element methods for design with adhesives." National Physical Laboratory.
- Fenner, R. T. (1988). *Mechanics of solids*, Blackwell Scientific Publications, Oxford [Oxfordshire] ;.
- Lam, L., and Teng, J. G. (2002). "Strength Models for Fiber-Reinforced Plastic-Confined Concrete." *Journal of Structural Engineering*, 128(5), 612-623.
- Lam, L., and Teng, J. G. (2004). "Ultimate Condition of Fiber Reinforced Polymer-Confined Concrete." *Journal of Composites for Construction*, 8(6), 539-548.
- Mirmiran, A. (1996). "Analytical and experimental investigation of reinforced concrete columns encased in fiberglass tubular jackets and use of fiber jacket for pile splicing." Florida Dept. of Transp., Tallahassee, Fla.

- Mirmiran, A., and Shahawy, M. (1997). "Behavior of Concrete Columns Confined by Fiber Composites." *Journal of Structural Engineering*, 123(5), 583-590.
- Tamuzs, V., Tepfers, R., You, C.-S., Rousakis, T., Repelis, I., Skruls, V., and Vilks, U. (2006). "Behavior of concrete cylinders confined by carbon-composite tapes and prestressed yarns 1. Experimental data." *Mechanics of Composite Materials*, 42(1), 13-32.
- Teng, J. G., Chen, J. F., and Smith, S. T. (2002). *FRP-strengthened RC Structures*, John Wiley and Sons.
- Teng, J. G., and Lam, L. (2004). "Behavior and Modeling of Fiber Reinforced Polymer-Confined Concrete." *Journal of Structural Engineering*, 130(11), 1713-1723.
- Vinson, J. R., and Sierakowski, R. L. (2002). *The Behavior of Structures Composed of Composite Materials*, Springer.

LONG-TERM MONITORING FOR SOIL NAILS AND ANCHORS BASED ON FBG SENSING TECHNIQUE

H. F. Pei¹, J. H. Yin¹, C. Y. Hong¹ and H. H. Zhu¹

¹Department of Civil and Structural Engineering,
The Hong Kong Polytechnic University, China. Email: 08902616r@polyu.edu.hk

ABSTRACT

There are many limitations of conventional techniques for slope monitoring including low accuracy, poor durability and difficulty of integration. This paper presents a new type of soil nails monitoring system basing on fibre Bragg grating (FBG) technique. In this study, a series of FBG sensors were installed onto the longitudinal surface (at specific interval) of soil nails and anchors for measuring the strain and temperature variation. Basing on the measured strain, the mechanical behaviour of soil nails can be evaluated, so that the slope stability can be further assessed. In addition, the advantages and limitations of the FBG based sensing technique in long term monitoring for soil nails are also discussed.

KEYWORDS

Slope, FBG, soil nail, strain and temperature, long-term monitoring.

INTRODUCTION

Soil nailing technique was widely used in monitoring the behaviour of geotechnical structures in last few decades. The stress state of geotechnical structures may vary as time elapse, especially for soil nails installed in slopes as a permanent reinforcement. This can be so the monitoring of soil nail is an effective method to reflect the actual stress conditions.

Conventional sensors have limitations in monitoring the performance of soil nails (Yin *et al.* 2007; Franzen. 1998; Schlosser. 1982), including low accuracy, interference by many factors easily, etc. To solve this problem, fibre Bragg Grating sensor (FBG) may become an alternative means in monitoring the strain distribution of soil nails in the long term. Wavelength shift of FBG sensor resulted from external temperature or strain change can be directly measured. Temperature compensation is achieved by encapsulating a loose FBG sensor into a copper tube. This sensor is only temperature sensitive so it can be named temperature sensor.

PRINCIPLE OF FBG SENSORS

In this project, FBG sensing technique is used for long-term monitoring of soil nails and anchors installed in a series of slopes. FBG sensors were installed onto the soil nails and anchors, temperature comprehension is also achieved by installing a series of temperature sensors.

Bragg grating is written into a segment fibre in which a periodic modulation of the core refractive index is formed. When a broadband source of light has been injected into the fibre, FBG reflects a narrow spectral part of light at certain wavelength, which is called the Bragg wavelength and dependent on the grating period and the refractive index of fibre (Morey, Meltz and Glenn 1989), this is Bragg's Law:

$$\lambda_B = 2n_{eff} \Lambda \quad (1)$$

where λ_B , n_{eff} , Λ , $\Delta\lambda$ and $\Delta\epsilon$ (e.g. Hill *et al.* 1978; Mendeza *et al.* 1990; Meltz *et al.* 1993; Idriss 2001) are the central wavelength of the sensor, (usually the wavelength range from 1510 to 1590nm) effective reflection ratio, distance from grating to grating.

The relationship between shift of wavelength and strain increment is as follows:

$$\frac{\Delta\lambda^\epsilon}{\Delta\epsilon} = c_\epsilon \Delta\epsilon + c_T \Delta T \quad (2)$$

where c_ϵ is the coefficient of strain measurement which is about $0.78 \mu\epsilon^{-1}$. When the temperature increment is ΔT , the increment of central wavelength of the sensor is:

$$\frac{\Delta\lambda_T}{\lambda_T} = c_T \Delta T \quad (3)$$

where $c_T = \alpha_f + \xi$ is about $6.67 \times 10^{-6} \text{ } ^\circ\text{C}^{-1}$, $\alpha_f = \frac{1}{\Lambda} \frac{d\Lambda}{dT}$ is the expansion coefficient of fibre, $\xi = \frac{1}{n} \frac{dn}{dT}$ is the

heat-light coefficient of optical fibre material.

In order to measure out the actual strain, the FBG sensor needs temperature compensation. If the environment temperature is constant, it is no need to add any temperature FBG sensor, so the formula can be changed to be shown as follows:

$$\varepsilon = \frac{\left(\frac{\Delta\lambda_{\varepsilon+T}}{\lambda_{\varepsilon+T}} - \frac{\Delta\lambda_T}{\lambda_T} \right)}{C_\varepsilon} \quad (4)$$

Sensors were calibrated before field applications. For the calibration of FBG sensors, digimatic gauges and translation stages on a research grade breadboard were used. 20 loading / unloading cycles were applied for every sensor to evaluate the fatigue effect. The surface mounted FBG sensors were glued to steel bars by epoxy, together with an electrical resistance strain gauge. A universal hydraulic servo-controlled machine was used to conduct tensile tests on the steel bar. To investigate the performance of FBG sensors used for temperature compensation, calibration tests were also carried out. Copper tubes with loose FBG sensors inside were merged into a temperature controllable water bath, together with a type-K thermocouple. A digital thermometer is used to measure the temperature variation during the tests.

Comparing the trend line equations the gauge factors C_ε and T_c of these sensors can be easily determined. For the bare, surface mounted and tube packaged FBG sensor, C_ε is 0.778. For the temperature sensor, $T_c = 6.37 \times 10^6 / ^\circ\text{C}$.

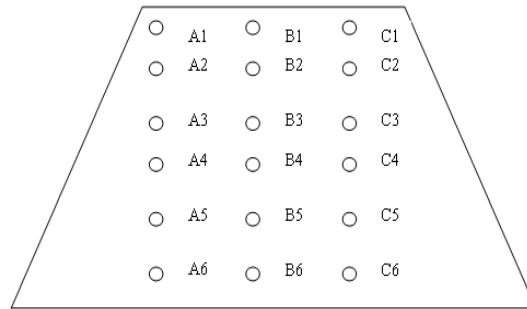
SOIL NAIL INSTRUMENTATION, TEST MEASUREMENT AND DATA ANALYSIS

Soil Nails Instrumentation

In this paper, a series of bare FBG sensors were adhered onto a pre-cut groove on the surface of soil nails and anchors covered by epoxy resin. Using such design, strain (axial force) distribution of soil nails can be evaluated, and a comprehensive analysis on the stability of soil nailed system can be carried out.



(a) Slope monitoring on site



(b) Positions of soil nails and anchors in the slope

Figure 1 soil nails monitoring distribution on the slope on site

Pan-Tian highway road locates in Panzhihua in Sichuan Province of China. These slopes were generally composed by completely decomposed granite, and the slope heights generally vary from 30 to 40 m. Soil nails and anchors were spaced at 1 m and installed in these slopes, anchors are 6m and 9m length, 6m anchors are A6, B6 and C6. 9m anchors are A5, B5 and C5.

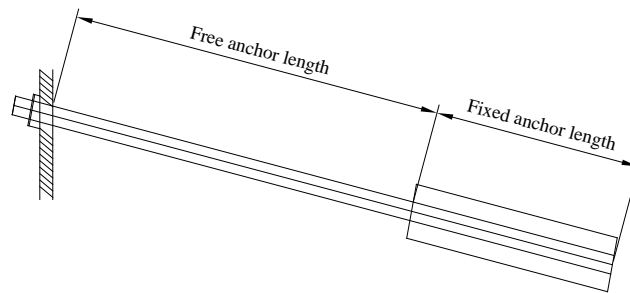
This slope is at the position: K188+775~K188+975 on Pantian highway road, the soil condition of this slope is full - strongly weathered granite, the length of it is 220m, the height of it is 42m, the slope is reinforced by beam, the hole of soil nails are 110mm in diameter. The number of soil nails monitoring in the slope is listed in Table 1. Installation is completed in July 2008, data were collected on July 2008, August 2008, September 2008, October 2008, February 2009 for four times.

The authors selected 18 soil nails in different positions of a slope for long term monitoring, Figure 1(a) shows a photo of the natural slope and Figure 1(b) shows the locations of installed soil nails. Figure 2 shows the schematic diagram of soil nail and anchor installed in slope.

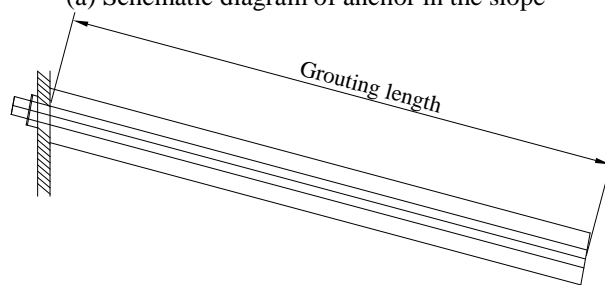
it is seen, three columns are chosen, namely section A, B, C. The soil nails and anchors from the top to the bottom were designated as A1~ A6, B1~ B6, C1~C6.

Table 1 Predicted-to-test bond strength ratios: bond strength models

Length of soil nails(m)	Number of soil nails and anchors	Diameter (mm)	Grouting length (m)	Pre-force (kN)
6	3	28	6	0
9	3	28	9	0
12	6	32	9	100
15	3	32	9	100



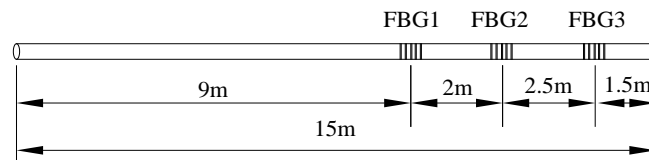
(a) Schematic diagram of anchor in the slope



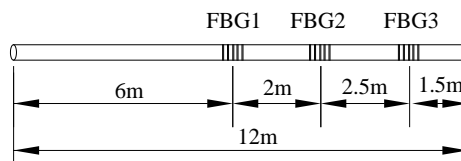
(b) Schematic diagram of soil nail in the slope

Figure 2 Schematic diagram of anchor and soil nail in the slope

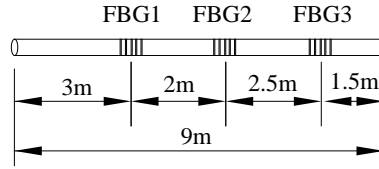
Data was collected after soil nails and anchors were installed with FBG sensors. Figure 3 show the locations of FBG on the steel bars. It is observed that, there are 3 strain sensors glued to the surface of steel bars, and one sensor used for temperature compensation in the same location.



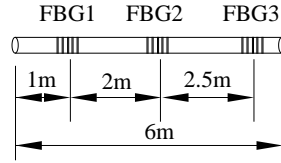
(a) Locations of FBG sensors on 15m length soil nail



(b) Locations of FBG sensors on 12m length soil nail



(c) Locations of FBG sensors on 9m length soil nail



(d) Locations of FBG sensors on 6m length soil nail



(a) Soil nails installed FBG sensors on site

Figure 3 soil nails and anchors monitoring on site and sensors distribution diagram

Data Analysis

The steel of rebar is HRB335 hot rolled ribbed steel bar, the mortar is of grade M30, generally steel rebar and concrete are considered as composite material, and the elastic modulus. (e.g. Yin *et al.* 2007; Franzen. 1998. Schlosser. 1982) is calculated by:

$$E_t = \frac{E_s A_s + E_c A_c}{A_s + A_c} \quad (5)$$

where E_t is the combination modulus of soil nail, E_s is the elastic modulus of steel rebar, E_c is the elastic modulus of concrete, A_s and A_c are the cross sectional area of steel rebar and concrete, respectively.

Where

$$A_c = A_t - A_s = \frac{\pi d_t^2}{4} - \frac{\pi d_s^2}{4} \quad (6)$$

where A_t is the area of hole, d_t is the diameter of holes is 110 mm, d_s is the diameters of steel rebar (32mm, 28mm).

The stress equilibrium on the soil nails and anchors is satisfied by:

$$E \cdot A \cdot \varepsilon_i = \tau \cdot \pi \cdot d \cdot l_a \quad (7)$$

The friction stress shown in Figure 4 is given by:

$$\tau = \frac{E \cdot A \cdot \varepsilon_i}{\pi \cdot d \cdot l_a} \quad (8)$$

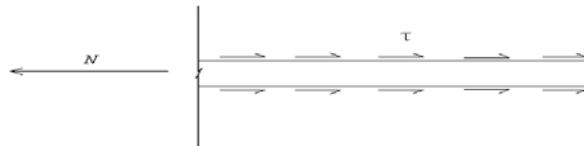


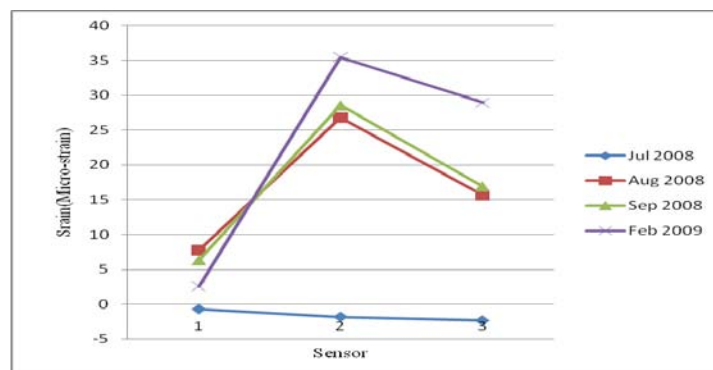
Figure 4 Schematic diagram of axial force equilibrium for soil nails and anchors

where E is the elastic modulus, ε_i is the number i strain value measured by the number i sensor, l_a is the anchor length of soil nail. The design pull-out force is 165kN.

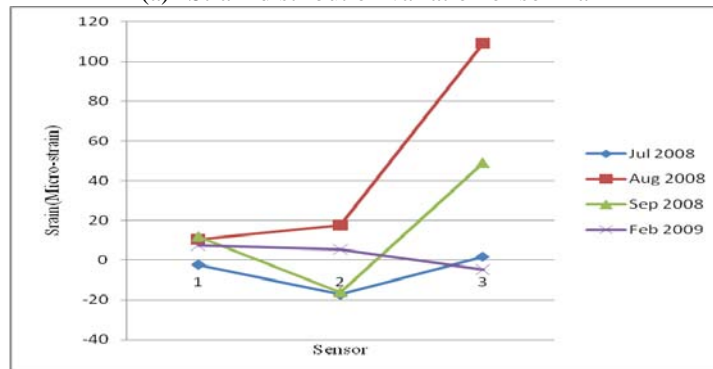
The maximum anchor force T_a is calculated by the follow formula:

$$T = \frac{T_f}{F_s} = \frac{\pi D L c}{F_s} \quad (9)$$

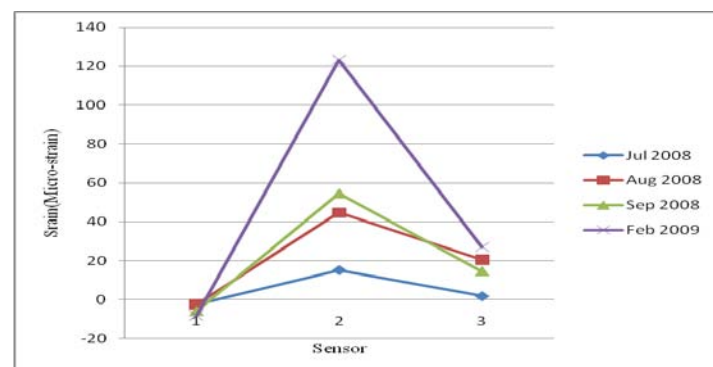
The author have chosen three cross sections including 18 soil nails and anchors, among them, in the first stage, soil nails are 6m and 9m in length, in the second stage, anchors are 12 m in length, for the third slope anchors are 15 metre length. Three strain sensors and one temperature sensor were installed on to the soil nails and anchors, the sensors on soil nail B4 were damaged in the process of slope reinforcement, others work well. Figure 5 shows the strain variations of soil nails and anchors A1, B5 and C1 as examples from July 2008 to February 2009. The strain results of soil nails and anchors appear to be stable.



(a) Strain distribution variation of soil nail A1



(b) Strain distribution variation of soil nail B1



(c) Strain distribution variation of soil nail C1

Figure 5 the strains of soil nails and anchors monitoring by FBG sensors

CONCLUSIONS

This paper presents a FBG based method to monitor long term behaviour of soil nails and anchors installed in slope. The maximum axial force of soil nail was calculated out by the method in this paper. The number of maximum axial force is 162.172kN which is less than the maximum anti-pullout force 165 kN of the soil nail designed by Highway Planning, Survey and Design Institute, the Department of Communication, Sichuan Province. This illustrates that all soil nails and anchors are safe. It was also observed in the present study that there are a few limitations while working with FBG sensors, like fragile material, small measuring range and bad compressive property. Thus, further study is needed.

ACKNOWLEDGMENTS

The authors gratefully acknowledge the financial support provided by the Research Grants Council of Hong Kong (Project No: B-Q12W)

REFERENCES

- Hill, K. O., Fujii, Y., Johnson, D. C., et al. (1978) "Photosensitivity in optical fiber waveguide: application to reflection fiber fabrication." *Applied Physics Letter*, 32(10): 647-649.
- Mendez, A., Morse, T., F., Mendez, F. (1990) "Applications of embedded optical fiber sensors in reinforced concrete buildings and structures". *Proc. of SPIE, Fiber Optic Smart Structures and Skins*, 1170: 60-69.
- Meltz, G., Morey, M. M., Gkenn, W. H. (1993) "Formation of Bragg Grating in optical fiber by UV expose through a phase mask." *Applied Physics Letter*, 62(10): 1035-1037.
- Meltz, G., Morey, W.W. and Glenn, W.H. 1989. Formation of Bragg gratings in optical fibers by a transverse holographic method. *Optics letter*, 14(15): 823-825.
- Idriss, R. L. (2001). "Monitoring of a smart bridge with embedded sensors during manufacturing, construction and service." *Proc. of 3rd International Workshop on Structural Health Monitoring*. Stanford University, 604-613.
- Yin, J. Zhu, H. H., Jin, W. (2007). "Performance evaluation of electrical strain gauges and optical fiber sensors in field soil nail pullout tests." *Geotechnical Advancements in Hong Kong since 1970s*, the HKIE Geotechnical Division 27th Annual Seminar. Hong Kong. 249-254
- Franzen, G. (1998). "Soil nailing-A laboratory and field study of pullout capacity." Doctoral thesis, Department of Geotechnical Engineering, Chalmers University of Technology, Sweden.
- Schlösser, F. (1982). "Behaviour and design of soil nailing." *Proc. on Recent Developments in Ground improvement Techniques*, Bangkok, Thailand: 399-413.

MEASUREMENT OF CRACKS IN CONCRETE BEAMS USING A BRILLOUIN OPTICAL TIME DOMAIN ANALYSIS SENSING TECHNOLOGY

C.Y. Hong¹, J. H. Yin¹, H. F. Pei¹, D. Huang¹

The Hong Kong Polytechnic University, Hong Kong. Email: joeyhcy@gmail.com

¹Department of Civil and Structural Engineering,
The Hong Kong Polytechnic University, China.

ABSTRACT

Brillouin optical time domain analysis (BOTDA) is considered as an effective health monitoring (long distance distributed strain and temperature measurement) technique for different structures such as pavements, buildings and oil pipes. In this paper, the BOTDA sensing technology is used for measuring cracks on small scale concrete beam. It is found from the experimental results that the existence of large tensile cracks in concrete beam can be identified with the BOTDA sensing technology. The measured strain increases faster after the tensile crack occurs at the bottom of the concrete beam. Based on the experimental study, the advantages of the fiber optic BOTDA sensing technology are: (a) the loop installation method is effective for strain measurement, and (b) large tensile cracks in concrete beam can be identified.

KEYWORDS:

BOTDA, small scale concrete beam, loop installation method, large tensile cracks.

INTRODUCTION

BOTDA sensing technique currently attracts extensive attention particularly in health monitoring for structures. Main advantages of BOTDA sensing technique are long distance measurement without sacrificing significant spatial resolution and low cost of the fiber optic BOTDA sensors. Additionally, the BOTDA sensors are remarkably strong, durable, thus easing the installation. In the practical application of the fiber optic BOTDA sensing technique especially for large structural monitoring, a considerable amount of local and global strain or temperature information can be obtained. Therefore, the potential problems of structures are effectively identified.

In the past few years, extensive theoretical studies have been carried out to investigate the influence of various parameters include the signal noise, sensors, performance of lasers and processing methods, *etc* on the spatial resolution of BOTDA technology (Horiguchi and Tateda 1989; Bao *et al.* 1993; Ruffin 2004; Kinzo *et al.* 2005; Ravet *et al.* 2006; Vedadi *et al.* 2007). Experimental investigations have also been performed to evaluate the feasibility of BOTDA sensing technology in practical application (Kwon *et al.* 2003; Kurashima *et al.* 2004; Nishio *et al.* 2007; He *et al.* 2008). Nowadays most researchers focused on the measurement of average strain distributions of different types of structures using BOTDA sensing technique (Kwon *et al.* 2002; Murayama *et al.* 2004; Niklesa *et al.* 2004; Hu 2007; Wu and Zhang 2007; Qian *et al.* 2008; Zhou *et al.* 2008). To date, an advanced technique namely Pulse Pre-Pump (PPP)-BOTDA technology was developed and applied for structural health monitoring by using optic fiber sensors (Nishio *et al.* 2007). The comparative high resolution enabled the technique to have great potential in identifying local defects or failures of structures.

Current study focuses on the crack identification of concrete beam using BOTDA sensing technique. Calibration method is introduced and adopted for calculating the actual strain results of different locations. Based on the typical test observations and measured results using BOTDA sensing technique, locations of the cracks occurred on a small scale concrete beam are identified. It is therefore recommended to apply the BOTDA sensing technique to estimate the crack locations of structures. However, the dimensions of cracks may be difficult to determine due to the limited resolution of BOTDA sensing technique and the uncertain number of cracks.

PRINCIPLE OF BOTDA

BOTDA sensing technique can be used for measuring the strain distribution by analyzing the spectrum characteristics of spontaneous Brillouin scattering of fiber optic sensors. Fig.1 shows a schematic view of the sensing principle of fiber optic BOTDA sensor. Two types of light include the pumping pulse light and continuous wave light launched from the two ends of fiber optic sensors interact with each other, then the pumping pulse light produces backward Brillouin gain when the continuous wave light frequency is different from the pump pulse light, but equivalent to the backward Brillouin frequency. Thus the continuous wave light will be amplified through Brillouin interaction and the backward Brillouin frequency will shift due to the strain or temperature variation of the optic fiber sensors. Brillouin frequency shift produced by temperature and strain are given as follows:

$$\nu(T) = \nu(0)(1 + C_T * T) \quad (1)$$

$$\nu(\varepsilon) = \nu(0)(1 + C_\varepsilon * \varepsilon) \quad (2)$$

where $\nu(\varepsilon)$ and $\nu(T)$ are the related frequency shift resulted from the strain and temperature changes, and can be directly obtained by BOTDA sensing device. $\nu(0)$ denotes the reference frequency. T and ε represent the changes of temperature and strain, while the relevant coefficients are defined as C_T and C_ε , respectively. Calibration setup and results of fiber optic BOTDA sensor will be introduced in the following section.

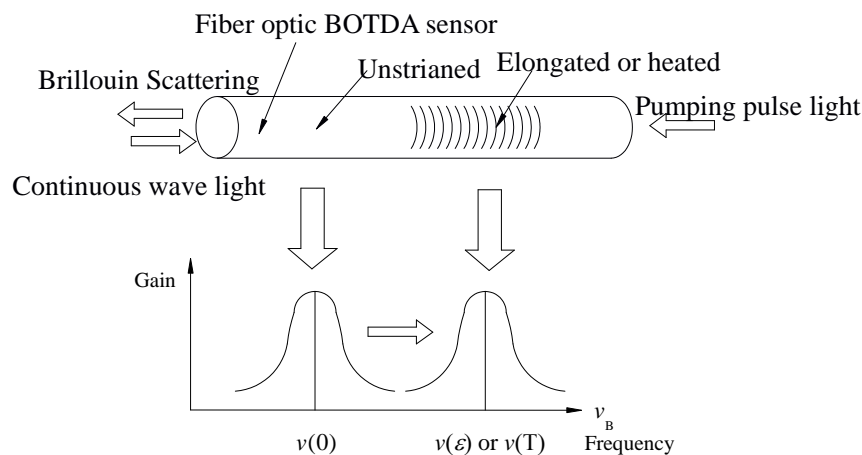


Figure 1 Schematic view of sensing principle of fiber optic BOTDA technique

THERMAL AND STRAIN CALIBRATION

Thermal calibration is essential to ensure the accuracy of repeatable measurement and can be performed by controlling or measuring the external temperature change with certified instruments. In this study, thermal calibration is carried out by heating the FBG and BOTDA temperature sensors inside water. Then the temperature variation measured by FBG temperature sensors was used to compare with that of fiber optic BOTDA sensors. Fig.2 shows a comparison of temperature measured by FBG and BOTDA sensors. A clear linear relationship is observed, and the slope ratio maintains at 1.

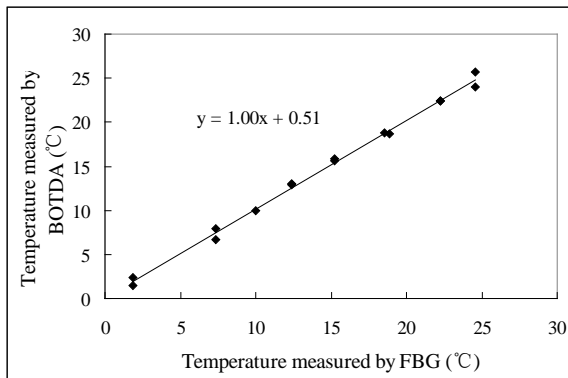


Figure 2. Comparison of temperature variations measured by BOTDA and FBG sensors

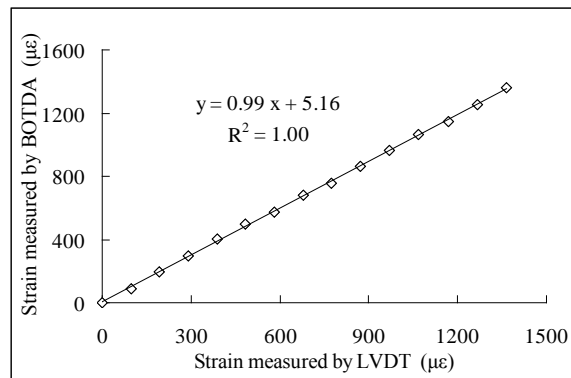


Figure.3 Comparison of strain variation measured by BOTDA and LVDT sensors

Strain calibration was conducted by applying tensile stress on bare fiber optic BOTDA sensor. The test was carried out by: (a) fixing the fiber optic sensor on an optical platform, which can be used for applying the tensile displacement on optical fiber sensor; (b) using linear variable displacement transducer (LVDT) to control and measure the tensile displacement that the fiber optic sensor encountered. It shall be noted that the special epoxy was used for fixing the fiber on the platform. Strain increment maintained around $100\mu\epsilon$, and the strain results of BOTDA sensors were immediately recorded after each strain increment was applied. The maximum tensile strain approached about $1600\mu\epsilon$. The minimum resolution of the LVDT sensors is $10^{-6}m$, which could ensure an accurate tension displacement. Fig.3 describes a comparison of strain variations measured by BOTDA and LVDT sensors. The figure clearly presents a linear relationship between the measured results of the two types of sensors. This typical relationship will be used for calculating the actual strain results of BOTDA sensors in practical application.

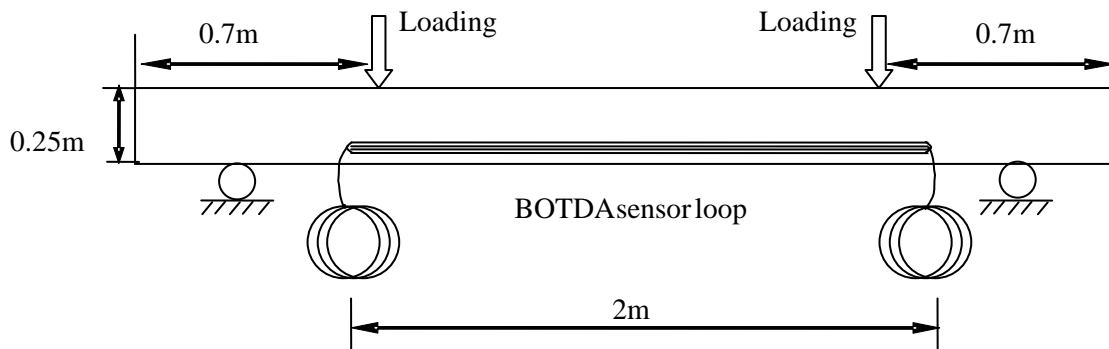


Fig.4 Schematic view of the loading test on concrete beam

CRACK IDENTIFICATION IN CONCRETE BEAM

A loading test was carried out on a small scale concrete beam, which has dimensions of 2.1m long, 0.15m width and 0.25m high. A schematic view of the experiment setup of the loading test is shown in Fig.4. Fiber optic BOTDA sensors were installed along the bottom of model concrete beam measuring the tensile strain produced by concentrate loadings. The loading locations were 0.7m away from the two ends of the upper surface of the beam (Fig.4). Strain results measured by BOTDA sensors were recorded immediately after each 2kN loading increment was applied. Fiber optic BOTDA sensors were installed using the loop installation method, which is simple and effective as each fiber loop can provide the fundamental strain or temperature information of structures (Wu and Zhang 2007).

Fig.5 shows the strain variations of four loops fiber optic BTODA sensors with the increase of load. It is clear that the average strain are initially small (less than $100\mu\epsilon$) and stable as loading varies from 2kN to 20kN (Figs.5 a and b). In this stage, the concrete beam is within elastic state, and the effect of varying load (from 2kN to 8kN) on the strain change is not obvious. As the load increases, strain results of different sensor loops are identified because different sensor loops measure the strain distributions of the same locations along concrete beam. Hence repeatable strain results were observed in Figs.5 b, c and d. Strain results of different fiber loops under

the same loading increment start to increase significantly after the loading approaches 22kN, then the strain develops much faster at greater load, particularly when the load achieves 30kN or the average strain approaches 180 $\mu\epsilon$ (Fig.5 c). This can be interpreted as that, cracks occurred in the locations where the ultimate tensile strain (about 180 $\mu\epsilon$) of concrete is achieved, leading to a significant strain concentration on the concrete surface. Ultimate tensile strain of the concrete beam was observed to be 8000 $\mu\epsilon$ at the load of 52kN (Fig.5 d). After this strain value, the optic fiber sensor damaged due to the presence of large tensile strain. It is therefore concluded that the fiber optic BOTDA sensor can bear large tensile strain. It is a good choice to measure large tensile strain of structures using the technique.

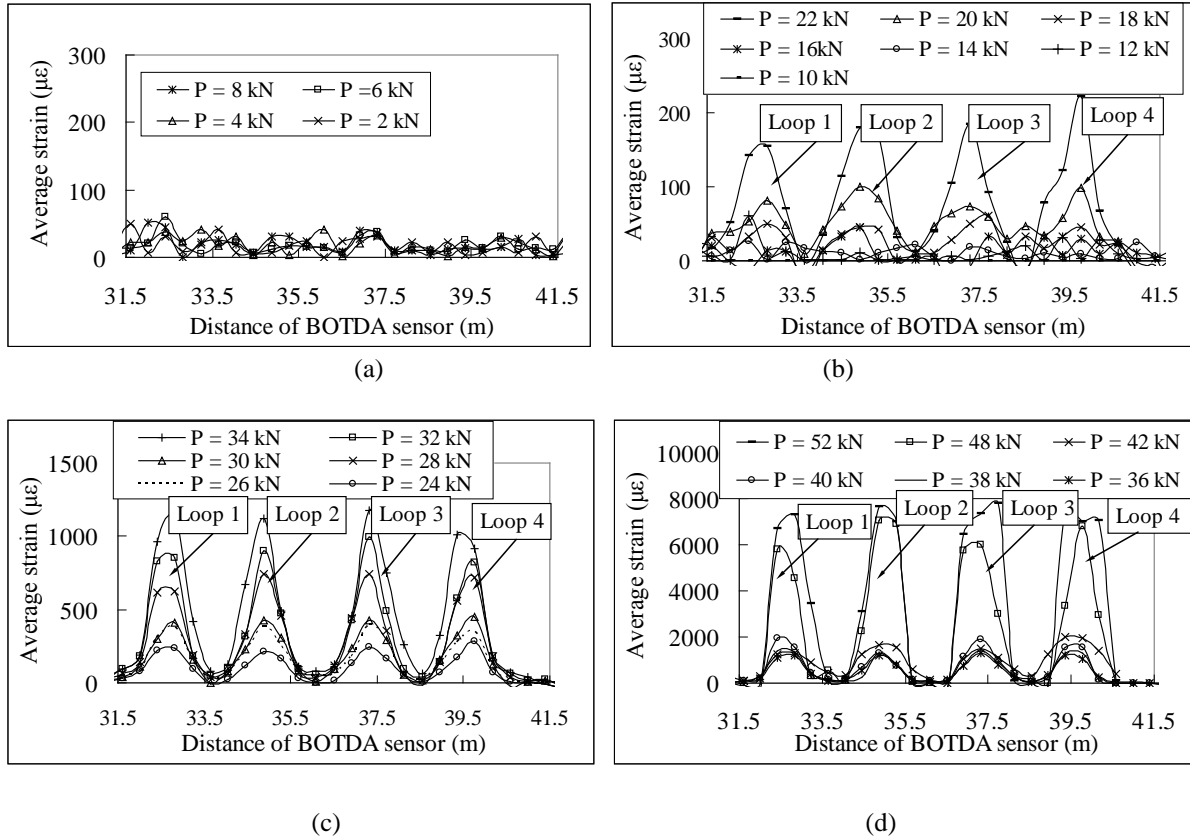


Figure.5 Average strain variations of BOTDA sensors when load varies from - (a) 2kN to 8kN; (b) 10kN to 22kN; (c) 24kN to 34kN; (d) 36kN to 52kN.

During the loading process, slightly strain differences between different loops of fiber optic BOTDA sensors under the same loading increment were observed (Figs.5 a b c d), indicating that the strain measured by different fiber loops are approximately equivalent. This is because the strain distribution of the same location of concrete is repeatedly measured by different fiber loops. In case the strain results of different fiber loops display scattered results, the cause may be due to the uncertainties in experimental setup or installation problem of the optic fiber sensor. Therefore, examination work should be carried out. In this way, the loop installation method ensures the reliability of the measured strain results.

Resolution of the BOTDA sensing technique is 0.4m, which implies that average strain of each 0.4m sensing length can be obtained. Figs.6 shows the variations of average strain with load at different locations of the fiber optic BOTDA sensors. It is observed that the strains are initially small under a comparative smaller load values. As the load increases, the BOTDA strain varies slightly when the load remains less than 22kN (or the measured strain is smaller than 180 $\mu\epsilon$). Afterwards, the strain develops much faster and approaches a much higher level especially for several specific distances along the fiber sensors such as 11.2-11.6m (Fig.6a) or 13.2-13.6m (Fig.6b), etc. The probable interpretation is that, there exists a threshold strain level which divides the boundary of elastic and damage state of the concrete beam. When the beam is within elastic state, the strain develops gradually and slowly with loading increment. But when the crack area occurs, the strain increases much faster.

Cracks occur as tensile strain approaches about 180 $\mu\epsilon$, leading to a significant strain concentration. Therefore, an dramatic strain increase was observed on the fiber optic BOTDA sensors. The locations where the average

strain are larger than $180\mu\epsilon$ can be considered as crack regions, such as the regions of 10.8~11.2m, 11.6~12.0m, and 12.4~12.8m (Fig.6a). Similarly, cracks were also found in the regions of 13.2~13.6m, 13.6~14.0m, 14.8~15.2m, 15.2~15.6m (Fig.6b). These cracks are roughly identified within a specific length (about 0.4m) due to the limited resolution of the BOTDA sensing technique. In addition, the crack width may be difficult to determine due to the uncertain number of the cracks presented in these regions. Locations of large tensile cracks will be further confirmed by observations from enlarged views of the concrete surface in the following section.

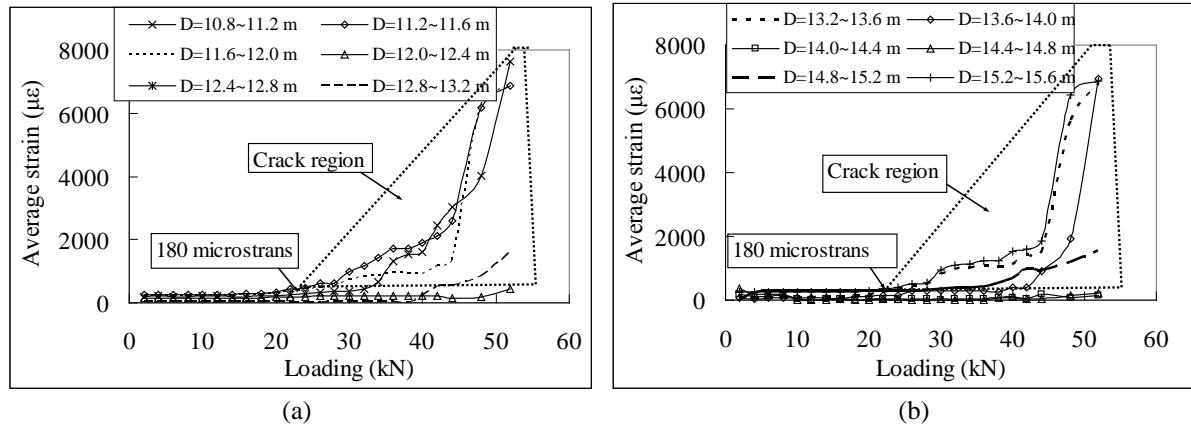


Figure 6. Variations of average strain with load on - (a) the first loop of fiber optic BOTDA sensor; and (b) the second loop of fiber optic BOTDA sensor.

Fig.7 describes the enlarged views of local cracks occurred at the bottom of the concrete beam under different loading levels at a distance of 10.8~11.2m on fiber optic BOTDA sensor. As crack width varies at 0.24mm, 0.28mm, and 0.63mm, significant debonding occurred at the interface between fiber optic BOTDA sensors and the concrete surface, but the BOTDA sensors were found to be still effective though a significant debonding from concrete surface was observed. This again confirms that the fiber optic BOTDA sensors can measure large tensile strain of structures. However, fiber optic BOTDA sensors were damaged immediately after $8000\mu\epsilon$ tensile strain was approached, indicating that the ultimate tensile strain of the bare optic fiber sensor is $8000\mu\epsilon$ in this test. Meanwhile, the relevant crack width occurred was measured to be 0.63 mm, which is close to the maximum crack width of 0.8mm that bare fiber can measure, as suggested by Qian *et al.* (2008).

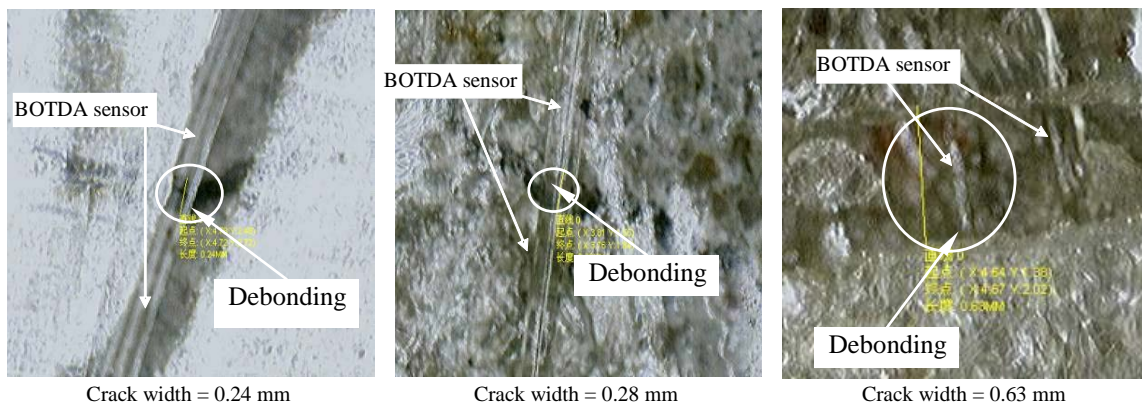


Figure 7. Enlarged views of cracks occurred on the concrete beam and the corresponding BOTDA sensors within the distance of 10.8~11.2m

It is noted that, the main limitation of bare fiber optic BOTDA sensor is the vulnerability as found in this study. The whole fiber can be damaged due to slight shearing effect. Therefore, it is quite time consuming to adhere fiber sensor on the concrete beam. In addition, the measurement may be failed if loop configuration is not formed, i.e., any damage to the fiber optic BOTDA sensor loop will result in a failed measurement. It is also noted that, if a fiber optic BOTDA sensor is well protected, the actual strain transferred from structures to the sensor shall be examined using calibration test. Therefore, particular attention should be paid on the protection skills of the bare fiber optic BOTDA sensors, as well as the actual strain transferred from the structures to the protected BOTDA sensors.

CONCLUSIONS

BOTDA is an effective sensing technology for distributed strain measurement. In this study, thermal and strain calibration methods were first introduced, then the performance of BOTDA sensing technology was examined by identifying the locations of cracks in an experiment carried out on a small scale concrete beam. The conclusions are drawn as follows:

- (a). Bare fiber optic BOTDA sensors can endure large tensile strain (about $8000\mu\epsilon$ as observed in the test), so that can be adopted for measuring large tensile deformation of structures.
- (b). Loop installation method of fiber optic BOTDA sensors is effective in monitoring tensile strain variation of structures as each sensor loop can provide independent strain results. Comparisons between different fiber loops can be adopted for examining the reliability of strain results.
- (c). The experiment carried out for crack identification using BOTDA sensing technique indicates that, the cracks occurred in concrete can be identified in a range of 0.4m. The resolution is sufficient, particularly in the health monitoring for large structures. But the crack width is difficult to determine due to the uncertain number of cracks.
- (d). Fiber optic BOTDA sensor is damaged after the maximum crack width approaches about 0.63mm, which is close to the crack width of 0.8 mm reported by previous researchers.

Main limitation of bare fiber optic BOTDA sensor is the vulnerability. In addition, the measurement can not be accomplished if the loop configuration failed to be formed, *i.e.*, any damage to the fiber loop will result in a failed measurement. Therefore, more attention should be paid on the protection measures of the fiber optic BOTDA sensors, as well as the actual strain transferred from structure to the BOTDA sensors.

ACKNOWLEDGMENTS

Financial support by a grant (PolyU 5320/07E) from the Research Grants Committee (RGC) of the Hong Kong Special Administrative Region Government of China and The Hong Kong Polytechnic University is acknowledged.

REFERENCES

- Bao X., Webb D.J. and Jackson D.A. (1993). "32-Km distributed temperature sensor based on Brillouin loss in an optic fiber", *Optics Letters*, 18(18), 1561-1563.
- He J.P., Zhou Z., Huang Y., Ou J.P. (2008). "Study on RC Beams using BOTDA(R)-FRP-OF technique", *Smart Sensors Phenomena, Technology, Networks, and Systems 2008, Proceedings of SPIE*, 69330U-1-69330U-7.
- Horiguchi T. and Tateda M. (1989). "BOTDA-Nondestructive measurement of single-mode optical fiber attenuation characteristics using Brillouin interaction: Theory", *Journal of Lightwave Technology*, 7(8), 1170-1176.
- Hu H.G. (2007). "Experimental research on layout techniques of BOTDA distributed optical fiber strain sensor", Thesis, Southeast University, China.
- Kinzo K., Li C.H., Kenichi N. (2005). "Pulse pre-pump method for cm-order spatial resolution of BOTDA", *17th International Conference on Optical Fibre Sensors, Proceedings of SPIE*, 5855.
- Kurashima T., Horiguchi T., Tateda M. (1990). "Distributed-temperature sensing using stimulated Brillouin-scattering in optical silica fiber", 15(18), *Optics Letters*, 1038-1040
- Kwon I.B., Baik S.J., Im K., Yu J.W. (2002). "Development of fiber optic BOTDA sensor for intrusion detection", *Sensors and Actuators A* 101, 77-84.
- Kwon I.B., Kim C.Y. and Choi M.Y. (2003). "Distributed strain and temperature measurement of a beam using fiber optic BOTDA sensor", *Smart Systems and Nondestructive Evaluation for Civil Infrastructures, Proceedings of SPIE*, 5057.
- Murayama H., Kageyama K., Naruse H., and Shimada A. (2004). "Distributed strain sensing from damaged composite materials based on shape variation of the Brillouin spectrum", *Journal of Intelligent Material Systems and Structures*, 15(1), 17-25.
- Niklesa M., Vogelb B., Briffoda F., Grosswigg S., Sausera F., Luebbeckeb S., Balsa A., Pfeifferb T. (2004). "Leakage detection using fiber optics distributed temperature monitoring", *Proceedings of the 11th SPIE Annual International Symposium on Smart Structures and Materials*, 18-25.
- Nishio M., Mizutania T., Takedaa N. (2007). "Structural shape identification using distributed strain data from PPP-BOTDA", *Proceedings of The Society of Photo-Optical Instrumentation Engineers*, 6530, 5301-5301.

- Qian Z.D., Huang W., Guan Y.S., Han G.Y. (2008). "Application of BOTDA on cracking monitoring for asphalt concrete pavement", *Journal of Southeast University*, 38(5), 799-803.
- Ravet F., Chen L., Bao X.Y., Zou L., Kalosha V.P. (2006). "Theoretical study of the effect of slow light on BOTDA spatial resolution", *Optical Express*, 14(22), 10351-10358.
- Ruffin A.B. (2004). "Stimulated Brillouin scattering: an overview of measurements, system impairments, and applications", *NIST-SOFM*, 2004, 1-5.
- Vedadi A., Alasia D., Lantz E., Maillotte H., Thévenaz L., González-Herráez M., and Sylvestre T. (2007). "Brillouin optical time-domain analysis of fiber-optic parametric amplifiers", *IEEE Photonics Technology Letters*, 19(2-4), 179-181.
- Wu Z.S., Zhang H. (2007). "A standard test method for evaluating crack monitoring performance of distributed fiber optic sensors", *proceedings of the 3rd international conference on structural health monitoring & intelligent infrastructure: structural health monitoring & intelligent infrastructure*, 585-593
- Zhou Z., He J.P., Yan K, Ou J.P. (2008). "Fiber-reinforced polymer-packaged optical fiber sensors based on Brillouin optical time-domain analysis", *Optical Engineering*, 47(1), 01440101- 01440110.